nature electronics

Article

https://doi.org/10.1038/s41928-025-01352-y

# A robust organic hydrogen sensor for distributed monitoring applications

Received: 26 January 2024

Accepted: 28 January 2025

Published online: 6 March 2025

Check for updates

Suman Mandal[1] ✉, Adam V. Marsh[1], Hendrik Faber[1], Tanmay Ghoshal[2], Dipak Kumar Goswami[3], Leonidas Tsetseris[4], Martin Heeney[1] & Thomas D. Anthopoulos[1,5] ✉

Hydrogen is an abundant and clean energy source that could help to decarbonize difficult-to-electrify economic sectors. However, its safe deployment relies on the availability of cost-effective hydrogen detection technologies. We describe a hydrogen sensor that uses an organic semiconductor as the active layer. It can operate over a wide temperature and humidity range. Ambient oxygen p-dopes the organic semiconductor, which improves hole transport, and the presence of hydrogen reverses this doping process, leading to a drop in current and enabling reliable and rapid hydrogen detection. The sensor exhibits a high responsivity (more than 10,000), fast response time (less than 1 s), low limit of detection (around 192 ppb) and low power consumption (less than 2 µW). It can operate continuously for more than 646 days in ambient air at room temperature. We show that the sensor outperforms a commercial hydrogen detector in realistic sensing scenarios, illustrating its suitability for application in distributed sensor networks for early warning of hydrogen leaks and preventing explosions or fires.

The unique properties of diatomic hydrogen ($H_2$), such as its rapid diffusion rate and high energy density, make it suitable for various applications in different industries, including energy, transportation, petroleum refining, defence, space, food and pharmaceuticals[1–4]. However, its combustible nature, low flammability point (approximately 4 vol% $H_2$ in the air) and the inability of people to detect it using their senses create safety concerns for hydrogen production, storage and usage[5]. There is, thus, a growing demand for sensitive and selective hydrogen sensors that can provide an early warning of potential leaks. To meet the large volume demands of the emerging hydrogen economies, such sensors must be cost-effective to manufacture, consume little power, operate at ambient conditions and have a minimal environmental impact. Among the different types of hydrogen sensors available, which include resistive, capacitive, optical, acoustic and magnetic systems[6–14], resistive-based technologies are arguably the most promising because they are simpler and more scalable to manufacture and can be integrated with incumbent electronics[15–20].

Various materials have been explored as the active element of such resistive hydrogen sensors to address the trade-offs between sensor performance (including sensitivity, rise time and fall time), shape, size, circuit complexity, power consumption and cost. These materials include noble metals such as palladium (Pd)[21] and oxide materials such as zinc oxide (ZnO), molybdenum trioxide ($MoO_3$), titanium dioxide ($TiO_2$), niobium pentoxide ($Nb_2O_5$), tin(IV) oxide ($SnO_2$), tungsten oxide ($W_2O_3$) and indium(III) oxide ($In_2O_3$)[6,22–27]. However, the typically low responsivity, high-temperature operation (requiring a power-hungry heating element) and long response time have limited their practical applications.

[1]Physical Science and Engineering Division, KAUST Solar Center (KSC), King Abdullah University of Science and Technology (KAUST), Thuwal, Saudi Arabia. [2]Department of Electronics and Electrical Communication Engineering, Indian Institute of Technology Kharagpur, Kharagpur, India. [3]Organic Electronics Laboratory, Department of Physics, Indian Institute of Technology Kharagpur, Kharagpur, India. [4]Department of Physics, School of Applied Mathematical and Physical Sciences, National Technical University of Athens, Athens, Greece. [5]Henry Royce Institute, Photon Science Institute, Department of Electrical and Electronic Engineering, The University of Manchester, Manchester, UK. ✉e-mail: suman.mandal@kaust.edu.sa; thomas.anthopoulos@manchester.ac.uk

https://doi.org/10.1038/s41928-025-01352-y

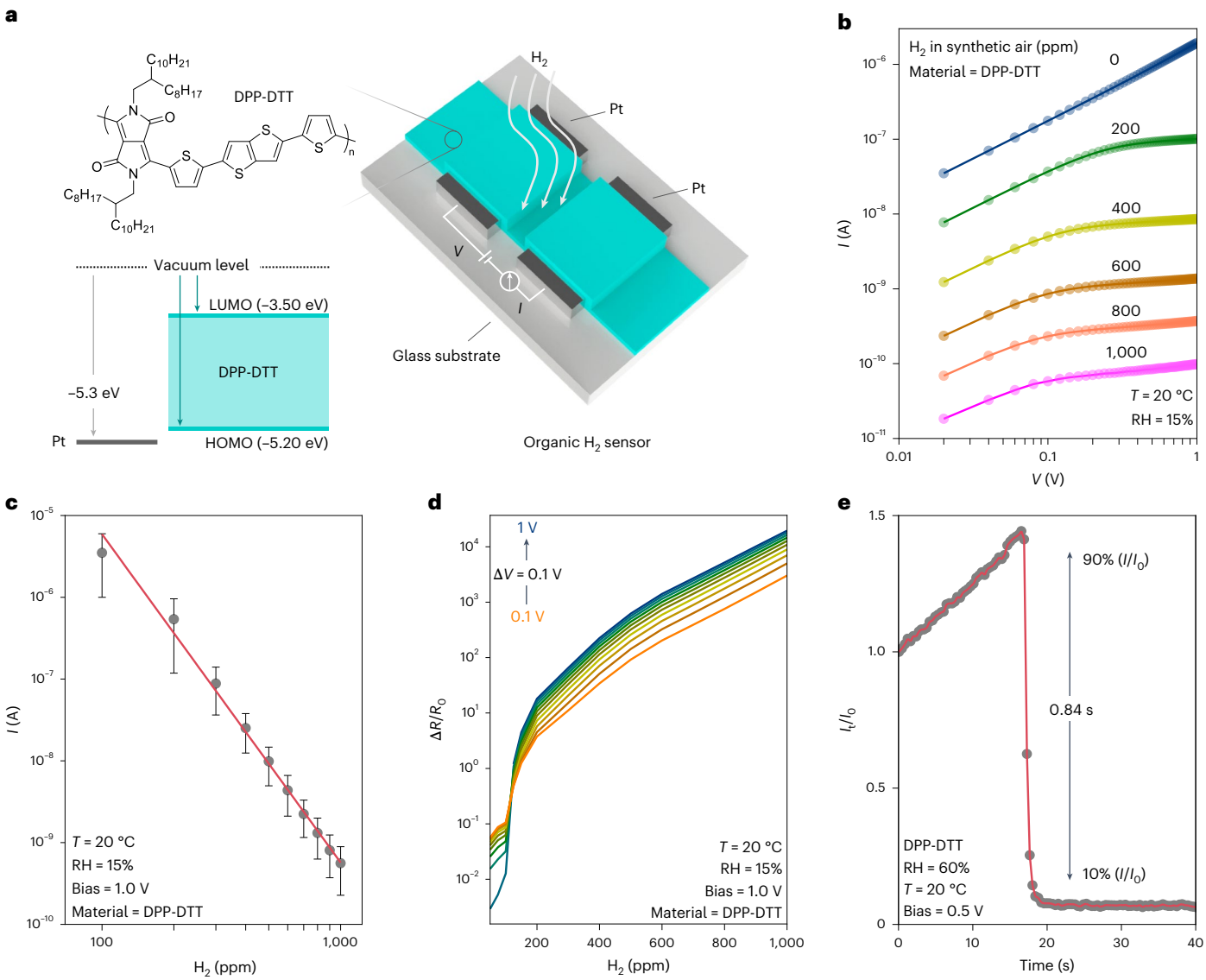


**Fig. 1 | Device schematic and characterization of $H_2$ sensing. a**, Schematic representation of the DPP-DTT-based $H_2$-sensing device composed (bottom to top) of glass, Pt and DPP-DTT. Also shown is the structure of DPP-DTT and a schematic representation of the energy levels of Pt and DPP-DTT with respect to the vacuum level. **b**, Current ($I$) versus voltage ($V$) curves of the sensing device were measured at various $H_2$ concentrations. **c**, $H_2$-concentration-dependent device current measured at a constant voltage of 1.0 V. The error bars indicate uncertainties in the device current mainly stemming from uncertainties in the thickness of the DPP-DTT thin films and represent the standard deviation from four individual devices. **d**, Change in responsivity ($\Delta R/R_0$) for various $H_2$ concentrations and for different biasing voltages applied to the device. **e**, Measurement of the fast $H_2$-dependent switching response for an applied bias of 0.5 V in ambient conditions (20 °C and 60% RH). Synthetic air was used as the carrier gas in the sensing measurements, as outlined in Methods. HOMO, highest occupied molecular orbital; LUMO, lowest unoccupied molecular orbital. $I_t$ and $I_0$ represent the measured device current over time and at $t = 0$ s, respectively.

Various metal composites[28–33] and organic materials, such as polypyrrole nanofibres and polyaniline[34–36], have also been investigated for $H_2$ detection. Polypyrrole nanofibre and polyaniline-based hydrogen sensors can exhibit a decrease in resistance with increasing hydrogen concentration due to the interaction with charged amine nitrogen sites on the polymers[36]. Pentacene-based organic field-effect transistors have also been employed to detect hydrogen by a different mechanism in which the contact resistance of the device at room temperature increases with the expansion of the palladium electrodes caused by the presence of hydrogen[37,38]. However, the suboptimal performance of these organic sensors in terms of sensing parameters, including low responsivity (≤0.9) and slow response time (up to 6 s), has impeded their deployment in practical applications.

In this article, we describe a hydrogen sensor that uses an organic semiconductor as the active layer. Our approach is based on the p-doping of organic semiconductors by oxygen species[39–41]. The current changes as a result of the interaction between hydrogen and the physisorbed oxygen species. The sensor offers high responsivity, fast response, low power consumption, low limit of detection (LoD) and good stability in harsh testing conditions. We also show that it can outperform a state-of-the-art commercial device in different practical sensing demonstrations.

## Sensor fabrication and performance

Our sensor has interdigitated platinum electrodes patterned lithographically (Fig. 1a, right and Extended Data Fig. 1) and a thin layer of the organic polymeric semiconductor poly[3,6-bis(5-thiophen-2-yl)-2,5-bis(2-octyldodecyl)pyrrolo[3,4-*c*]pyrrole-1,4(2H,5H)-dione-2,2'-diyl-alt-thieno[3,2-*b*]thiophen-2,5-diyl] (DPP-DTT) deposited on top by spin-coating or printing (Fig. 1a, left). The polymer forms a conformal

and smooth layer with a root mean square surface roughness of ~0.6 nm (Extended Data Fig. 1). Before the polymer layer was deposited by photoelectron spectroscopy, the work function of the platinum electrode was measured to be 5.3 eV (Extended Data Fig. 1), which matches well with the highest occupied molecular orbital energy level of DPP-DTT of −5.2 eV, making it a good hole-injecting contact. Completed devices were stored in dry air inside a dry box for 10 h before testing. The device was then transferred into a test chamber and exposed to a stream of synthetic air mixed with varying concentrations of $H_2$ following the experimental procedures described in Methods (Extended Data Fig. 2).

Figure 1b shows the current versus voltage characteristics of the optimized device (Supplementary Fig. 1) recorded before and after exposure to hydrogen for a few minutes at room temperature. Under 100% synthetic air (0 ppm $H_2$), a linear current versus voltage ($I$–$V$) characteristic was recorded, indicating the presence of Ohmic conduction under equilibrium conditions. Upon inserting various amounts of $H_2$ from 100 to 1,000 ppm, the sensor current decreased logarithmically by 10,000-fold from microampere to sub-nanoampere levels (Fig. 1c) at room temperature and under 1.0 V bias, demonstrating its high sensitivity to $H_2$. Such a drastic current decrease can be attributed only to carrier depletion induced upon exposure to $H_2$. The current reduction in the low-voltage regime (0–0.1 V) was followed by a second conduction regime (>0.1 V), manifested as a sublinear $I$–$V$ dependence. Qualitatively similar $I$–$V$ characteristics have previously been attributed to Schottky barriers at both contacts in two-terminal semiconductor diodes[42]. We hypothesize that ambient oxygen p-dopes the DPP-DTT and shifts the Fermi energy so that the Pt/DPP-DTT becomes more Ohmic while the device conductivity increases (Extended Data Fig. 3). Exposure to $H_2$ gas de-dopes the organic semiconductor and reduces its work function, giving rise to a higher Schottky barrier at each Pt–organic semiconductor interface to form a back-to-back diode equivalent circuit. Modulating the Schottky barriers by p-doping and subsequent de-doping leads to the strong current modulation observed in the $I$–$V$ characteristics (Fig. 1b and Extended Data Fig. 4a) due to its exponential dependence on the barrier height.

The $H_2$ concentration-dependent responsivity, defined as $\Delta R/R_0$, where $R$ is the electrical resistance at the measured $H_2$ concentration, and $R_0$ is the resistance before $H_2$ exposure, was calculated from the $I$–$V$ characteristics for an applied bias between 0.1 and 1.0 V (Fig. 1d, Extended Data Fig. 4b and Supplementary Fig. 2). We found that the responsivity at higher hydrogen concentrations (1,000 ppm) saturated at around 1.0 V. Accordingly, 1.0 V was chosen for further temporal hydrogen response measurements at higher hydrogen concentrations. A bias-dependent $\Delta R/R_0$ of more than six orders of magnitude was observed upon increasing the $H_2$ concentration from 100 to 1,000 ppm. The signal evolution at constant $H_2$ concentrations recorded at 0.5 V, shown in Extended Data Fig. 4c, confirms the robust sensing behaviour of the device. The extracted LoD of the DPP-DTT sensor was approximately 192 ppb (Extended Data Fig. 4b).

The dynamic response of the sensor was studied next by subjecting the DPP-DTT device to pulses of synthetic air containing different $H_2$ concentrations (Extended Data Fig. 4d) inside the gas-sensing chamber, which was maintained at 20 °C with 15% relative humidity (RH). Exposure of the sensor to 1% $H_2$ (10,000 ppm) yielded a notably fast signal response with a rise time of ~0.84 s (Fig. 1e). The rapid response to hydrogen was also demonstrated by leaking hydrogen gas (99.99%) close to the organic sensor (Supplementary Video 1). The longer-term stability of the sensing process was confirmed by recording the response of the sensor over 1,000 sensing cycles at 0.1% $H_2$ (1,000 ppm) (Extended Data Fig. 4e). A statistical analysis of the rise and fall times yields 0.83 (±0.08) s and 6.52 (±0.21) s, respectively (Extended Data Fig. 4f). These results demonstrate the excellent sensing capabilities of the organic device, which surpass most hydrogen sensor performance metrics as defined by the US Department of Energy and those published in the literature (Supplementary Table 1)[43–45].

## Mechanism of hydrogen detection

The proposed macroscopic and atomic-level mechanism for hydrogen sensing in our device is presented in Fig. 2a (left and right, respectively). In step (i), the organic sensor is introduced into an oxygen-containing environment (for example, ambient air) and is p-doped by oxygen molecules. This leads to an increase in the device current, and the biasing leads to the catalytic formation of oxygen adatoms on the surface of the Pt electrodes. In step (ii), hydrogen is introduced and immediately permeates through the organic semiconductor. In step (iii), the hydrogen molecules are split at the electrodes into adatoms and subsequently react with oxygen adatoms to form water. This reduces the oxygen-induced doping and is accompanied by a fast reduction in the device current, so that hydrogen is detected. The water molecules formed leave the device through evaporation, and the current remains low as long as hydrogen is present. In step (iv), the device remains exposed to ambient air although hydrogen exposure has ceased. Oxygen again p-dopes the organic semiconductor, leading to a rapid increase in the current (signal recovery) and the cessation of hydrogen sensing.

To verify the proposed sensing mechanism, we undertook a series of density functional theory (DFT) calculations (Extended Data Fig. 5). The calculations targeted several processes and corresponding molecular structures involving oxygen- and hydrogen-related species in the bulk of the organic semiconductors of interest, as well as at the surface of the Pt electrode. We first examined the stability of oxygen molecules next to polymer chains of DPP-DTT and two other organic semiconductors, namely poly(indacenodithiophene-co-benzothiadiazole) ($C_{16}$-IDTBT) and poly(3-hexyl)thiophene (P3HT) (Extended Data Fig. 5a,b). In all cases, we found that it is energetically favourable for an oxygen molecule to dissociate and form sulfonyl groups on the polymers (other O-chemisorbed structures are also stable, but their energies are higher than that of the sulfonyl configuration). However, as shown in a previous DFT study[41], the activation energy for the process of a physisorbed $O_2$ molecule next to a P3HT polymer chain reacting together to create a sulfonyl group on the thiophene is very high (approximately 2.0 eV). Hence, this process is largely suppressed in our device, and any oxygen molecules that have diffused into the bulk of P3HT (or DPP-DTT or $C_{16}$-IDTBT, which have similar S-based heterocyclic groups) will probably remain as $O_2$ in physisorbed configurations (Fig. 2b). Interestingly, density of states (DOS) calculations of the corresponding structures revealed that physisorbed $O_2$ molecules create unfilled energy states inside the bandgaps and close to the respective valence bands of DPP-DTT, P3HT and $C_{16}$-IDTBT. Figure 2c shows the DOS results for DPP-DTT. The results for P3HT and $C_{16}$-IDTBT are presented in Extended Data Fig. 5a,b. The existence of these acceptor states is consistent with the effect of p-doping of oxygen on the polymers of interest (as well as other typical organic semiconductors)[46,47].

Having identified the physisorbed oxygen molecules as the source of p-doping, we next aimed to understand the processes that enable the de-doping of the organic semiconductors in the presence of $H_2$. The first mechanism considered was that hydrogen molecules react directly with physisorbed $O_2$ molecules. We probed such a scenario with DFT-nudged elastic band (DFT-NEB) calculations and found that the transformation of physisorbed $H_2$ and $O_2$ into an $H_2O$ molecule and an S-O group on a P3HT polymer chain is an exothermic process with a prohibitively high energetic barrier of 2.50 eV. Another possibility was that hydrogen molecules reacted with O species chemisorbed on the polymer. However, as we mentioned earlier, the formation of such species is also suppressed due to their very high activation energies.

As the barriers to reactions involving $O_2$ in these organic polymers are high, an alternative scenario focuses on the role of the Pt electrodes. It is known that Pt is efficient in dissociating hydrogen molecules and creating atomic H adatoms on its surface[48]. Accordingly, we performed a series of DFT-NEB calculations to investigate reactions of such H adatoms with O species on a Pt surface. The corresponding results are

https://doi.org/10.1038/s41928-025-01352-y

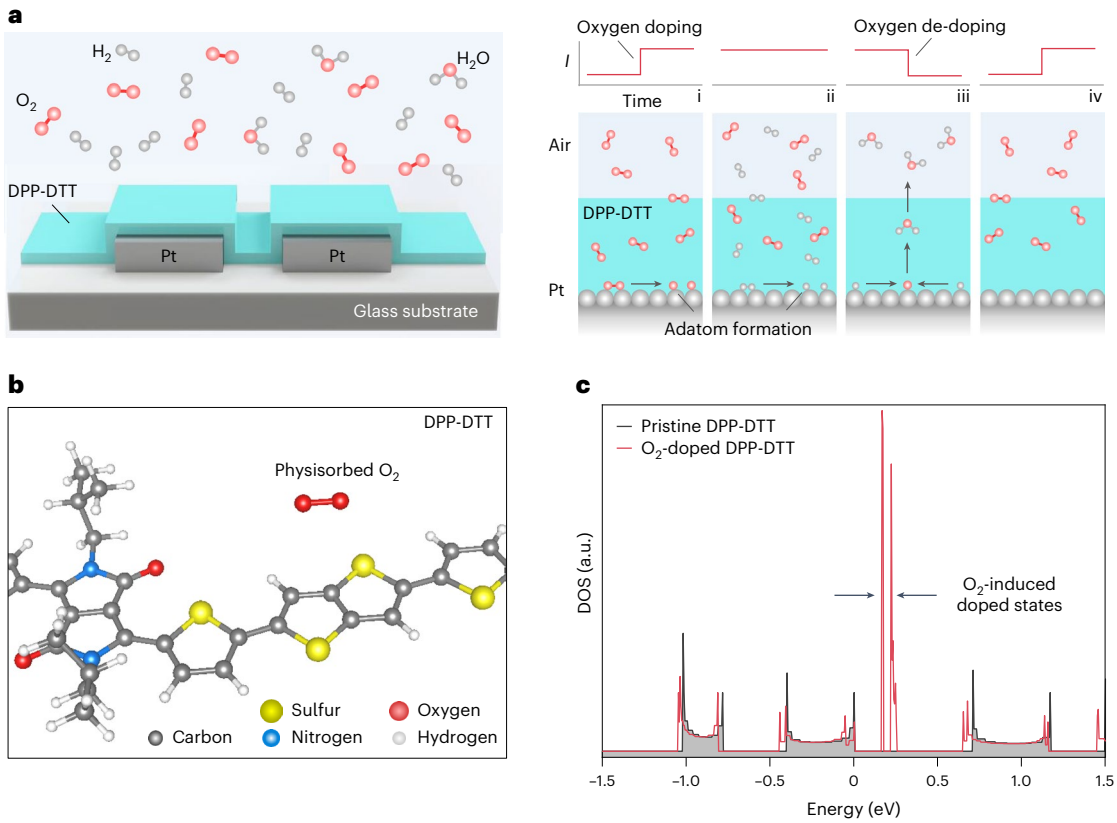


**Fig. 2 | Working principle of the device and theoretical data. a**, Schematic representation of the $H_2$-sensing device and the hydrogen-sensing mechanism through oxygen doping and de-doping processes. **b**, DPP-DTT polymer chain with a physisorbed $O_2$ molecule. **c**, Electronic DOS for the pristine DPP-DTT polymer (grey-shaded region) and the $O_2$-physisorbed configuration (red line). The energy of the highest occupied state was set to zero. The $O_2$-induced peaks above zero (above the valence band maximum) confirm that physisorbed $O_2$ molecule dopants can act as acceptors for the DPP-DTT polymer.

presented in Extended Data Fig. 5c–f. From these results, we deduce that, first, oxygen molecules are chemisorbed on the Pt surface, and then, in a multistep process, H adatoms react with the O adatoms to create $H_2O$ molecules. The latter have relatively small binding energies to the surface (0.2 eV), so some of these molecules will desorb. This process of eliminating p-type dopant oxygen species from the organic semiconductor in the presence of hydrogen leads to a reduction in current, as observed in our devices. To verify the role of the Pt electrode, a DPP-DTT device was prepared with gold (Au) electrodes. The experimental results (Supplementary Fig. 3) indicate that the DPP-DTT device did not show any significant response in the presence of hydrogen with Au electrodes, suggesting that the catalytic effects of Pt are crucial to the working mechanism of the device.

Finally, to exclude the possibility of electrochemical effects, we used a mixed ionic–electronic conductor, poly(3,4-ethylenedioxythiophene) polystyrene sulfonate, which exhibits high ionic conductivity like that of organic electrolytic materials, as the sensing layer (Supplementary Fig. 4). The high ionic conductivity overwhelmed the effect of oxygen p-doping, so that the device did not respond to hydrogen, which supports our conclusion regarding the resistive nature of our organic sensors.

## Stress testing the organic hydrogen sensor

To investigate whether the p-doping and de-doping processes by $O_2$ and $H_2$, respectively, could be observed in other organic semiconductors, we studied several other hole-transporting organic semiconductors: $C_{16}$-IDTBT, P3HT, 6,13-bis(triisopropylsilylethynyl)pentacene (TIPS-pentacene), poly[bis(4-phenyl)(2,4,6-trimethylphenyl)amine] (PTAA) and one electron-transporting material, namely 2,2'-((2Z,2'Z)-((12,13-bis(2-ethylhexyl)-3,9-diundecyl-12,13-dihydro-[1,2,5]thiadiazolo[3,4-e]thieno-[2",3":4',5']thieno[2',3':4,5]pyrrolo[3,2-g]thieno-[2',3':4,5]thieno[3,2-b]indole-2,10-diyl)bis(methanylylidene))-bis(5,6-difluoro-3-oxo-2,3-dihydro-1H-indene-2,1-diylidene))dimalononitrile (Y6). The detailed analysis of the response to hydrogen exposure for all sensors developed is presented in Fig. 3a and Extended Data Fig. 6a–d. The DPP-DTT sensor exhibited the highest responsivity of over three orders of magnitude, while the P3HT device showed the lowest. The Y6-based sensor had a low current due to the poor electron injection caused by the large mismatch of the Pt work function with the lowest unoccupied molecular orbital and highest occupied molecular orbital levels of Y6. The sensor showed no evidence of oxygen-induced p-doping and no response to $H_2$ (Extended Data Fig. 6e). These findings also provide further support to the proposed sensing mechanism that relies on $O_2$-induced p-doping and the subsequent de-doping upon exposure to hydrogen. Due to its superior performance among the range of active-layer materials tested, the DPP-DTT sensor was chosen for further analysis.

The performance of the DPP-DTT sensors was evaluated under different environmental conditions, such as elevated temperatures, different interfering volatile gases and varying RH (Fig. 3b–f). A small increase was observed in the responsivity up to 40 °C for $H_2$ concentrations up to 800 ppm (Fig. 3b). However, the responsivity of the sensor decreased on increasing the temperature from 60 to 120 °C. We attribute this to the lower adsorption rate for oxygen[49] and $H_2$ at higher temperatures[50]. Figure 3c shows the real-time response of the sensor to $H_2$ concentrations from 0 to 1,000 ppm at 120 °C, which demonstrates its robust sensing capabilities even under such harsh conditions (full sets of the sensing characteristics of the DPP-DTT sensor measured at various temperatures from 40 to 120 °C are shown in Extended Data Fig. 7a–e). We also studied the long-term thermal stability of the DPP-DTT devices

https://doi.org/10.1038/s41928-025-01352-y

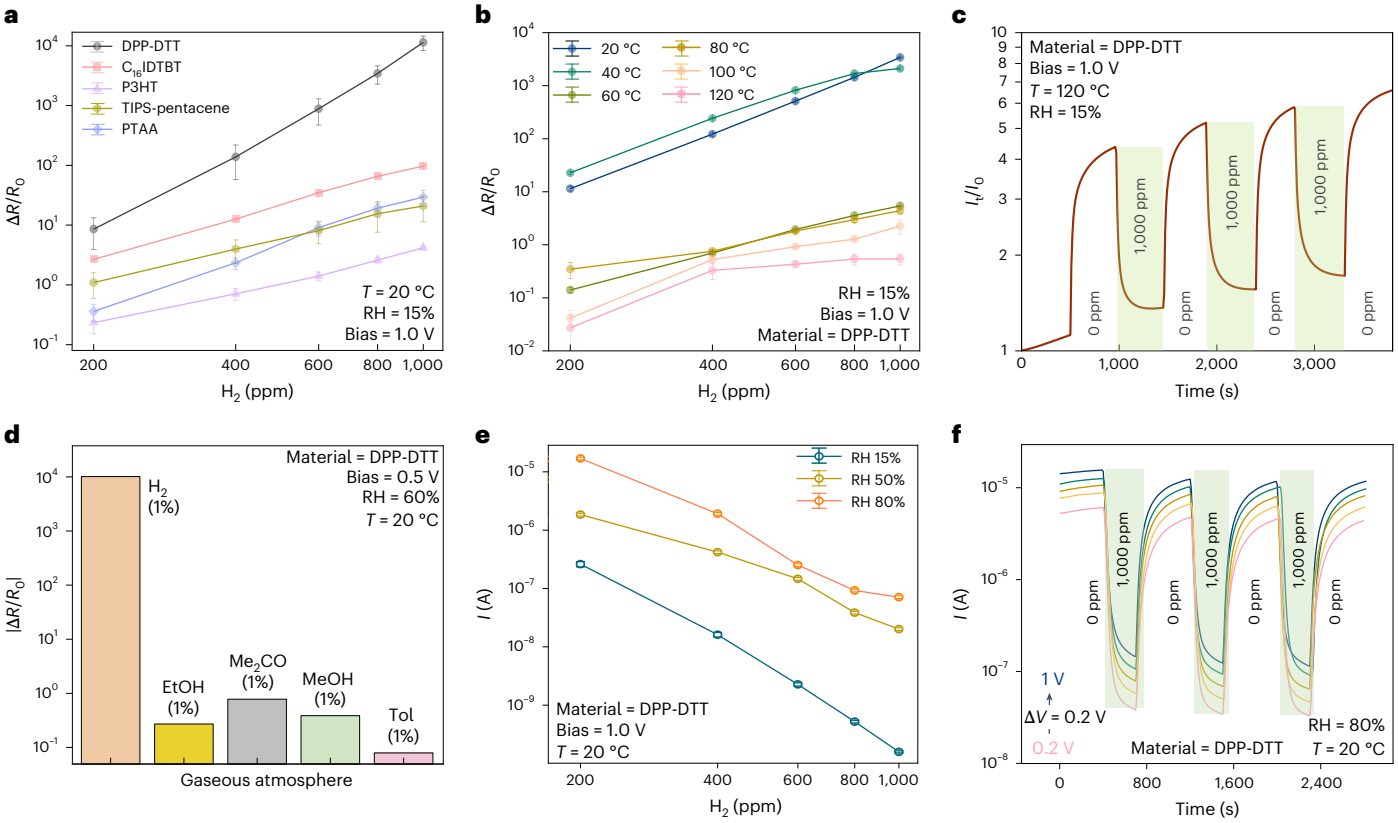


**Fig. 3 | Performance characteristics of different organic-based hydrogen sensors under various conditions. a**, $H_2$ concentration-dependent device responsivity of the organic materials DPP-DTT, $C_{16}$-IDTBT, P3HT, TIPS-pentacene and PTAA. The error bars define the standard deviation of the mean responsivity by averaging over three different devices for each material. **b**, Temperature-dependent responsivity of the DPP-DTT $H_2$ sensor. The error bars indicate the standard deviation in the responsivity from the mean from four different sets of data taken from a single device. **c**, Real-time current as a function of $H_2$ concentration from 0 to 1,000 ppm at 120 °C for an applied bias of 1.0 V. **d**, Change in the responsivity of the DPP-DTT sensor in the presence of individual gases measured at a constant bias of 0.5 V and a concentration of 1% (10,000 ppm). **e**, Hydrogen concentration-dependent current of the DPP-DTT device, measured under various humidity conditions (15%, 50% and 80% RH). The error bars denote the standard deviation in the device current from the mean from four different sets of data taken from a single device. **f**, Real-time current response of the DPP-DTT device measured at various applied bias conditions (0.2 to 1.0 V in 0.2 V increments), as a function of switching the $H_2$ concentration from 0 to 1,000 ppm at an 80% RH. Except for **d**, synthetic air was the carrier gas in all experiments, as outlined in Methods. EtOH, ethanol; MeOH, methanol; $Me_2CO$, acetone; Tol, toluene.

(Supplementary Fig. 5) and found that their response to hydrogen, in terms of current change, remained largely independent of thermal stress. Thus, the organic sensor does not require extended stabilization periods before it can be used for quantitative $H_2$ concentration measurements.

The selectivity of the DPP-DTT sensor to $H_2$ was also examined in the presence of various volatile organics (interfering species), including ethanol, methanol, acetone and toluene, which exhibit flammability and reducing properties like those of hydrogen and are commonly found in household environments[51] (Fig. 3d and Extended Data Fig. 8a). The change in absolute responsivity for $H_2$ was approximately four orders of magnitude higher than that for the other compounds, even in a lower responsivity region (0.5 V), indicating the possibility of a further reduction in the power consumption of the organic hydrogen sensor. In further experiments, the DPP-DTT organic device did not exhibit any response to non-volatile reducing methane gas (0.1% in air) when measured at 20 °C and 15% RH (Supplementary Fig. 6). The current response of the DPP-DTT sensor was also examined in the presence of the oxidizing-gas nitrogen dioxide. The oxidation of the DPP-DTT layer produced holes that increased the device current, in contrast to the effect observed with $H_2$ (Supplementary Fig. 7). However, the device did not return to its initial state due to persistent conductivity and exhibited a very slow recovery, probably due to the irreversible oxidation of DPP-DTT. Importantly, the sensor was able to detect the presence of $H_2$ in a complex gas mixture containing 1.0% $H_2$, 1.0% $O_2$, 1.0% $N_2$ and 1.0% $CO_2$ in Ar (Extended Data Fig. 9a). Before $H_2$ exposure, the sensor showed a slight increase in the current when exposed to a stream of Ar gas containing 10% $CO_2$ and $O_2$ (Extended Data Fig. 9b,c); however, these small changes occurred at different timescales and did not interfere with the ability of the sensor to detect the presence of $H_2$ rapidly in real time (Extended Data Fig. 9d).

The organic sensor showed no response when balloons filled with Ar, $N_2$ and dry air were popped under the same experimental conditions to simulate sudden changes in the stoichiometry of the ambient atmosphere (Extended Data Fig. 10d), highlighting the specificity of the sensor to $H_2$. The performance of the hydrogen sensor was also examined under atmospheric (21%) and high (99.9%) oxygen conditions for comparison. The corresponding *I*–*V* characteristics were measured at hydrogen concentrations of 0 and 1,000 ppm (Supplementary Fig. 8). We found that under 99.9% $O_2$ conditions, the device current increased for both 0 and 1,000 ppm hydrogen concentrations. However, the device current remained largely unchanged despite the fourfold increase in $O_2$ concentration, indicating that the responsivity of the device in various $O_2$ environments remained unaffected. The only condition where the sensor failed to recover was when the atmosphere lacked $O_2$. Extended Data Fig. 9e,f shows that the sensor response to $H_2$ when inert gases were used as the carrier (Ar or $N_2$) was initially strong, but its signal failed to recover due to the absence of $O_2$, which is responsible for the subsequent p-doping.

https://doi.org/10.1038/s41928-025-01352-y

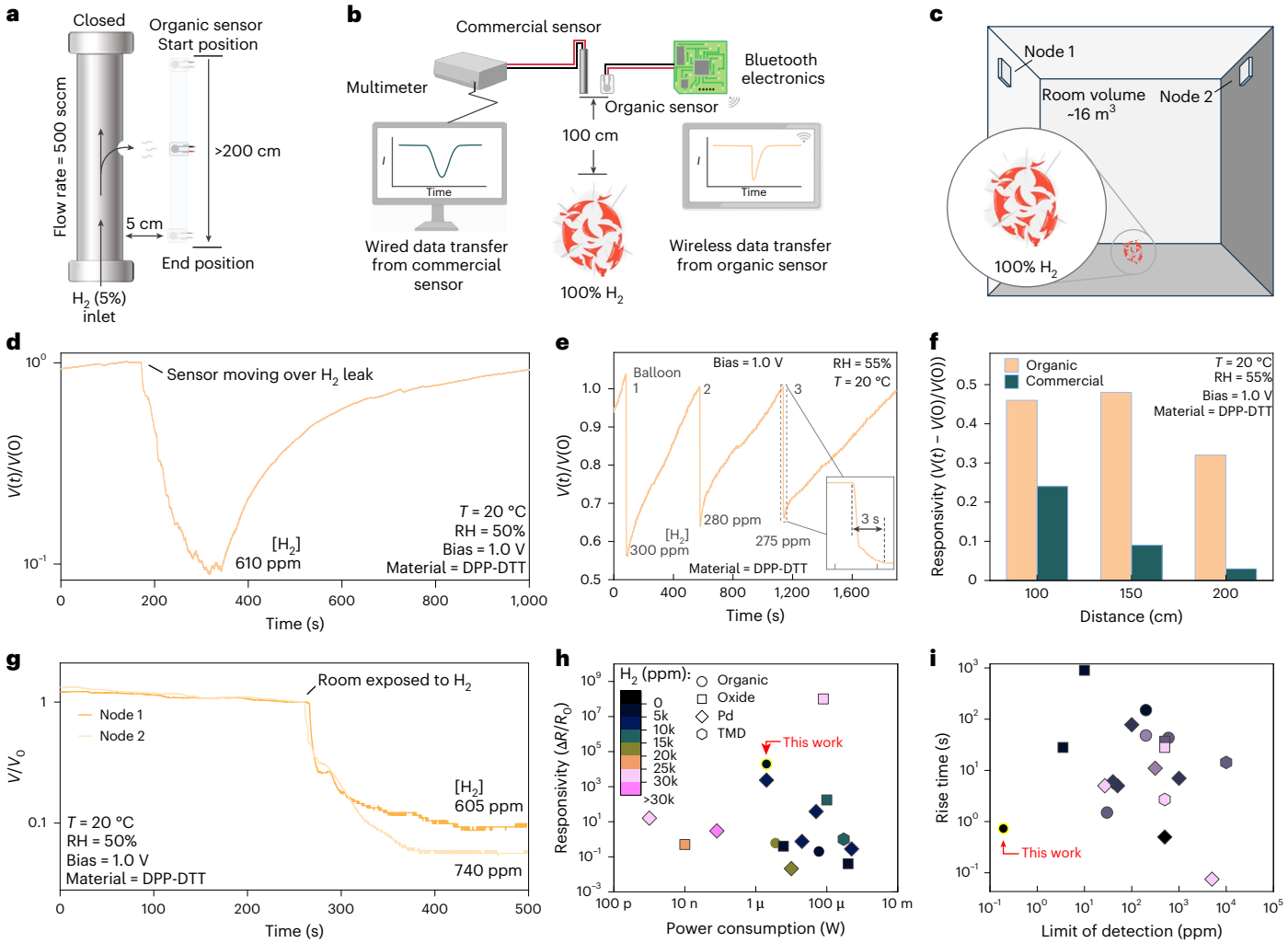


**Fig. 4 | Evaluation of the response of the organic hydrogen sensor in different sensing scenarios and comparisons with a commercial sensor. a**, Schematic illustration of the measurement set-up for the $H_2$ leak detection system. An organic sensing unit was moved slowly towards the hydrogen-exposed region to detect the hydrogen concentration leaking from a pipe carrying hydrogen gas. The data were wirelessly transmitted to a smartphone. **b**, Schematic illustration of the experimental set-up of an early warning system. A wireless organic DPP-DTT sensor was used to detect a simulated $H_2$ leak. A balloon containing 100% $H_2$ placed at various distances below the sensor was popped in a controlled, closed-room environment to simulate the leak. **c**, Schematic of the experimental set-up for wirelessly monitoring $H_2$ concentration inside a closed room, which had two sensing nodes on opposite walls. Approximately 15 l of 100% $H_2$ were released onto the floor and allowed to diffuse throughout the room. **d**, Temporal hydrogen response of the DPP-DTT sensor in terms of normalized voltage when detecting a hydrogen leak, as shown in **a**. **e**, Real-time response of the organic DPP-DTT sensor to repeated $H_2$ leaks simulated by sequentially bursting three balloons 100 cm from the sensor. **f**, Comparison of the responsivity of the commercial and organic sensors calculated from the balloon-popping experiments. **g**, Time-dependent normalized voltage variations at nodes 1 and 2 when detecting hydrogen inside the room, as shown in **c**. **h**,**i**, Comparison of responsivity versus power consumption (**h**) and rise time versus the LoD (**i**) for various organic, oxide, Pd and transition-metal dichalcogenide based resistive hydrogen-sensing devices reported in the literature in the last two decades (Supplementary Table 2). sccm, standard cubic centimetres per minute; TMD, transition-metal dichalcogenide. Schematic in **b** was created with BioRender.com.

To determine the impact of humidity on the $H_2$-sensing capabilities of the device, we conducted measurements across a range of RH from 15% to 80% for various $H_2$ concentrations ranging from 0 to 1,000 ppm (Fig. 3e and Extended Data Fig. 8b–d). The hydronium ions in water doped the organic semiconductor, such that the device current increased with humidity, as reflected in the $I$–$V$ characteristics. In the presence of hydrogen, the organic semiconductor was de-doped, causing a decrease in the device current. However, hydrogen adatoms also react with hydroxyl ions, so that the device current increased and the hydrogen response reduced as the humidity was increased. The device exhibited robust dynamic operation with more than two orders of magnitude of current change upon repeated exposure to 0 and 1,000 ppm of $H_2$ at 80% RH for various bias conditions ranging from 0.2 to 1.0 V in 0.2 V increments (Fig. 3f). In long-term stability testing of the device under high humidity conditions (80% RH), the device was found to be stable (Supplementary Fig. 9). Finally, the long-term stability of the DPP-DTT sensors was studied by storing them in ambient air and humidity (20–24 °C and 50–60% RH) while sporadically testing their response to 1,000 ppm of $H_2$ under controlled conditions of 20 °C and 15% RH at 1 V. These data are plotted in Extended Data Fig. 10e. The sensor remained functional for nearly 2 years (646 days), with its response plateauing after an initial 'burn-in' period of ~60 days.

Our experiments demonstrate that the organic hydrogen sensor meets most of the target specifications for hydrogen safety applications. These include signal responsivity (0.25 relative resistance at 1% $H_2$), LoD (<0.1%), response speed ($t_{90}$ < 1 s at 1% $H_2$), recovery speed ($t_{10}$ < 60 s) and cost (potentially well under US$40 per unit), as defined by the US Department of Energy and in the literature

(Supplementary Table 1)[43–45]. $t_{90}$ is defined as the time required for the device current or resistance to change from 10% to 90% in the presence of hydrogen, while $t_{10}$ is the time taken for the device current or resistance to change from 90% to 10% in the absence of hydrogen. This led us to investigate the practical utility of this technology in realistic sensing applications, which we will discuss next.

## Quantitative hydrogen sensing in practical scenarios

Before deploying the sensor in the quantitative detection of $H_2$ in practical scenarios, the device was calibrated with hydrogen concentrations ranging from background levels (500 ppb) to 1,000 ppm in ambient conditions (~20 °C and ~50% RH) using the same measuring electronics used in the demonstrations (Supplementary Fig. 10). We then studied the capability of the organic sensor to detect $H_2$ under three sensing scenarios.

In the first scenario, the sensor acted as a dynamic leak detector (Fig. 4a) tasked to monitor the $H_2$ concentration leaking from a pipe connected to a cylinder containing 5% $H_2$ in synthetic air under ambient conditions. The leak was controlled by a mass-flow controller. Throughout the experiment, we maintained a flow rate of 500 standard cubic centimetres per minute. The sensing unit was slowly moved by hand. A rapid reduction of the current was observed as it was moved through the leak area, corresponding to a $H_2$ concentration of 610 ppm (Fig. 4d).

In the second scenario, we used the sensor as a warning system for $H_2$ leaks inside a closed room (volume ~18 $m^3$, at room temperature and 55% RH) and compared its response with a commercial hydrogen sensor (details in Methods). $H_2$-filled balloons were placed 100 cm below the sensor unit and popped with a needle, as shown in Fig. 4b. The response of the organic sensor was recorded wirelessly in real time. Figure 4e shows the response signal from the organic sensor from the three sequentially burst balloons. The hydrogen concentrations measured by the organic sensor were 300 ppm (balloon 1), 280 ppm (balloon 2) and 275 ppm (balloon 3). The organic sensor exhibited a fast response of ~3 s, which was maintained even after several consecutive balloon bursts (inset in Fig. 4e). Extended Data Fig. 10c shows the real-time signals from both the commercial and organic sensors at distances of 100, 150 and 200 cm from the bursting balloon. In each case, the organic sensor exhibited a faster and larger response than the commercial sensor. Moreover, the responsivity of the organic sensor was almost double that of the commercial sensor (Fig. 4f). The results indicate that, as a hydrogen-sensing unit (electronics together with sensor), the wireless organic sensor demonstrates better device performance in terms of responsivity compared to the wired commercial apparatus.

In the third scenario, two sensing nodes (nodes 1 and 2) were deployed at different positions inside a closed room (volume ~16 $m^3$) with a ventilation system (Fig. 4c). The sensors were positioned on opposite walls, approximately 2.5 m apart. Supplementary Fig. 11 is a photograph showing the dimensions of the room. Approximately 15 l of 100% hydrogen were released from several popped balloons placed on the floor of the room. The distances from the hydrogen source to nodes 1 and 2 were approximately 3.0 and 2.2 m, respectively. The released $H_2$ gas diffused throughout the room, and its concentration was monitored wirelessly in real time by the two nodes (Fig. 4g). The hydrogen concentrations measured at nodes 1 and 2 were approximately 605 and 740 ppm, respectively. This simple yet powerful demonstration shows the potential for these organic detectors to be used in wireless sensor networks.

The organic sensor was even used in a quantitative analysis of $H_2$ concentration under dynamic conditions. Specifically, the wireless sensor was mounted on a drone and quantitatively detected the hydrogen concentration while flying through an area where an $H_2$ leak had just occurred (Supplementary Fig. 12). The measured hydrogen concentration was approximately 320 ppm. Similarly, its high-fidelity dynamic sensing capability was also observed in a water-splitting experiment. Several cycles of $H_2$ generation were monitored with an average rise time of 14 (±4) s (Extended Data Fig. 10a,b and Supplementary Video 2). The extracted hydrogen concentration in the exhaust gas (Extended Data Fig. 10b) was ~335 ppm, as determined from the calibration curve in Supplementary Fig. 10 using a measured RH of ~52% at 20 °C (Supplementary Fig. 13). The dynamic response of the organic sensor was also compared against that of the commercial sensor by monitoring the evolution of $H_2$ concentration during a chemical reaction between Mg and acetic acid inside a round-bottom flask (Supplementary Fig. 15). The organic sensor showed faster response and recovery times than the commercial device.

Finally, to investigate the potential for cost-effective fabrication of these devices, we used a screen-printing process to deposit DPP-DTT onto interdigitated Pt electrodes and measured the performance of the devices (Supplementary Fig. 14a,b). The responsivity of the screen-printed devices was comparable to devices prepared by spin-coating, thus demonstrating that this technology is amenable to cheap, high-throughput manufacturing. Compared to other sensor technologies (Fig. 4h,i and Supplementary Table 2), our organic hydrogen sensor has the potential to be simpler to manufacture with superior performance (higher responsivity, lower power consumption and so on) and thus offers a promising technical solution for the safe and widespread use of hydrogen technologies.

## Conclusions

We have described a reversible hydrogen-induced de-doping mechanism in organic semiconductors, which we used to develop a robust hydrogen sensor. The organic sensor exhibits a high responsivity ($1.19 \times 10^4$), fast response time (<1 s), low power consumption (≤2 μW; with no requirement for an external heating element), low LoD (~192 ppb), stability in harsh testing conditions and high selectivity for hydrogen even in complex gas environments. We also showed that our organic hydrogen sensor can outperform a commercial device in different practical sensing demonstrations. With its potential for scalable and cost-effective fabrication due to the attractive properties of organic semiconductors, our hydrogen sensor could be of widespread use in the emerging hydrogen economy.

## Methods

### Interdigitated electrodes

Titanium (50 nm)/platinum (150 nm) interdigitated electrodes with 5-μm gaps (IDE2) patterned on a glass substrate were purchased from Micrux and used as electrodes. All IDE2 samples were cleaned by ultrasonication in water, isopropanol and acetone for 5 min each before depositing the organic semiconductor.

### Active materials

This work used the following organic semiconducting materials: DPP-DTT, $C_{16}$-IDTBT, P3HT, TIPS-pentacene and Y6. DPP-DTT, P3HT and TIPS-pentacene were purchased from Ossila, and PTAA and Y6 were purchased from 1-Material. All commercially supplied materials were used as received without further purification. $C_{16}$-IDTBT (Mn 65 kg $mol^{-1}$, dispersity of a polymer (Đ) 2.4) was synthesized in our laboratory.

### Material preparation

DPP-DTT (5 mg $ml^{-1}$, chlorobenzene), $C_{16}$-IDTBT (6 mg $ml^{-1}$, chlorobenzene), P3HT (8 mg $ml^{-1}$, chlorobenzene), PTAA (8 mg $ml^{-1}$, chlorobenzene), TIPS-pentacene (5 mg $ml^{-1}$, toluene) and Y6 (10 mg $ml^{-1}$, chlorobenzene) were dissolved overnight on a hotplate at 70 °C while being stirred at 1,000 rpm. The DPP-DTT solution was spin-coated at 4,000 rpm for 60 s on the interdigitated Pt electrodes, followed by annealing at 100 °C for 90 min. $C_{16}$-IDTBT, P3HT, PTAA and Y6 were spin-coated at 2,000 rpm for 60 s on the interdigitated Pt electrodes, followed by annealing at 100 °C for 90 min. The TIPS-pentacene solution (10 μl) was drop cast onto the interdigitated Pt electrodes and annealed at 50 °C for 5 min. The thicknesses of the different organic

semiconducting layers, measured with a stylus surface profilometer (Bruker), were 21 (±5), 32 (±6), 42 (±9), 49 (±8), 32 (±5) and 463 (±42) nm for DPP-DTT, $C_{16}$-IDTBT, P3HT, PTAA, Y6 and TIPS-pentacene, respectively.

### Characterization

All hydrogen sensors were electrically characterized inside a Linkam HFS600E-PB4 chamber. The equilibrium of the gas flow was achieved with two mass-flow controllers (ALICAT). The temperature of the sensing device inside the chamber was varied to study the temperature-dependent $H_2$ sensing. All the electrical characterization measurements were obtained with Agilent B1500A instruments. Custom MATLAB programs were used to control the mass-flow controllers when mixing and diluting the sensing gas according to experimental requirements. This program was also used to provide hydrogen in pulsed form on top of the sensing surface, and this process was employed to evaluate the response of the device. The response from the other volatile gases (not $H_2$) was measured using the DPP-DTT device inside a custom-designed chamber. For the response measurements, a particular amount of ethanol, methanol, acetone or toluene was soaked in tissue paper and placed in the chamber to achieve a 1% environment of each gas. A DHT11 humidity sensor, which has a measuring accuracy of ±5%, was used to calibrate the humidity inside the gas-sensing chamber (Linkam) as well as the ambient humidity level for all the humidity-dependent $H_2$-sensing measurements. A commercially available Pt Clark-type electrode-based $H_2$-detecting system (Unisense, approximately US$1,200 per electrode) was also used to detect $H_2$. We compared its response with that of our organic hydrogen-sensing device. The surface morphology of the DPP-DTT-coated interdigitated Pt electrode was studied using an atomic force microscope (NT-MDT) in tapping mode. The work function of the Pt electrodes was measured by photoelectron spectroscopy in air using RIKEN KEIKI equipment. Gas cylinders were purchased from either Abdullah Hashim Industrial Gases & Equipment or Air Liquide. The responsivity of the sensor to hydrogen gas was calculated as $(R - R_0)/R_0$, where $R_0$ is the device current (or resistance) before hydrogen exposure and $R$ is the device current after exposure to air containing 1,000 ppm $H_2$. The LoD of the DPP-DTT device was extracted from a linear fit of the $H_2$ concentration-dependent responsivity curve using 3.3 × (standard deviation of the intercept/slope of the linear curve), where the standard deviation of the intercept = (number of data points used in the measurement times the standard error of the intercept). The power consumption of the sensor was calculated as $P = V \times I$, where $V$ is the bias applied to the device and $I$ is the measured sensing current.

### DFT methodology

DFT studies were carried out with the Vienna Ab Initio Simulation Package[52] using a plane-wave basis (with an energy cutoff of 400 eV), projector augmented waves[53], the generalized gradient approximation for Perdew–Burke–Ernzerhof[54] exchange-correlation functional and the DFT-D3 method for the van der Waals interactions[55].

To simulate the effect of oxygen and hydrogen reactions with the polymers of interest, we modelled them with a single periodic chain. The sampling of the reciprocal space in calculations of the electronic DOS used the tetrahedron method with 18 $k$-points in the direction of the periodic chain[56]. The structures were rendered with the software VESTA[57]. The activation energies of pertinent processes were obtained with the nudged elastic method[58], which models the so-called minimum energy pathway as a 'chain' of subsequent configurations (termed images) along the reaction coordinate.

### Proof-of-concept demonstrations

We have demonstrated hydrogen sensing in three example use cases: hydrogen-generating chemical reactions, water electrolysis and the bursting of a $H_2$-filled balloon. We used prototype electronics[59] with the organic sensor to send sensing data wirelessly to an Android mobile phone, which analysed the data in real time. Photographs of the circuit layout and the printed circuit board used for the measuring electronics are shown in Supplementary Fig. 16. In these demonstrations, a commercial hydrogen sensor from UNISENSE was used for comparison. Its low power consumption (~2 µW) makes the organic sensor suitable for safe hydrogen detection applications as this reduces the risk of sparking. The organic sensor can detect hydrogen concentrations well below the flammable range (>40,000 ppm), enabling pre-emptive security alerts before hydrogen reaches hazardous levels.

To demonstrate the detection of hydrogen from chemical reactions (Supplementary Fig. 15), a three-necked 500-ml round-bottom flask equipped with a condenser and two septa was charged with a mixture of magnesium shavings (20 g) and water (50 ml). The top of the condenser was fitted with the DPP-DTT organic sensor and the commercial hydrogen sensor, and a continuous flow of air was introduced through one of the septa. Once the responses of the sensors had become stable, 1 M aq. acetic acid (0.1 ml) was added through the other septum. Data from both sensors were simultaneously recorded as the response to the generated hydrogen. After hydrogen evolution ceased, another portion of the aqueous acetic acid was added, and this process was repeated several times.

For the water hydrolysis experiments, we designed a small reaction chamber made of glass. We used steel springs as electrodes inside the chamber. Further, 2.5 M aq NaOH was used as the electrolyte. The spring electrodes were partially covered with small cylindrical plastic pipes, which collected $H_2$ and $O_2$ from the cathode and anode electrodes, respectively. The reaction chamber was connected to a 9.0 V battery (Duracell). Data from the organic sensor were recorded remotely by the bespoke electronics.

The balloon-bursting experiments were performed at room temperature in ambient air. The 100% hydrogen-filled balloons were placed at varying distances (100–200 cm) from the organic and commercial hydrogen sensors at stationary positions. The balloons were then burst using a sharp needle, and the response from the two sensors was recorded simultaneously in real time.

## Data availability

Source data are provided with this paper. All other data supporting the findings of this study are available from the corresponding authors upon reasonable request.

## References

1. Sharma, S. & Ghoshal, S. K. Hydrogen the future transportation fuel: from production to applications. *Renew. Sustain. Energy Rev.* **43**, 1151–1158 (2015).
2. Ramachandran, R. & Menon, R. K. An overview of industrial uses of hydrogen. *Int. J. Hydrogen Energy* **23**, 593–598 (1998).
3. Ge, L., Yang, M., Yang, N. N., Yin, X. X. & Song, W. G. Molecular hydrogen: a preventive and therapeutic medical gas for various diseases. *Oncotarget* **8**, 102653–102673 (2017).
4. Narayana Das, J. in *Energy Engineering* (eds Raghavan, K. V. & Ghosh, P.) 9–18 (Springer, 2017).
5. Hubert, T., Boon-Brett, L., Black, G. & Banach, U. Hydrogen sensors – a review. *Sens. Actuators B* **157**, 329–352 (2011).
6. Yang, P. Y. et al. Fast, sensitive, and highly selective room-temperature hydrogen sensing of defect-rich orthorhombic $Nb_2O_{5-x}$ nanobelts with an abnormal p-type sensor response. *ACS Appl. Mater. Interfaces* **14**, 25937–25948 (2022).
7. Jo, M. S. et al. Wireless and linear hydrogen detection up to 4% with high sensitivity through phase-transition-inhibited Pd nanowires. *ACS Nano* **16**, 11957–11967 (2022).
8. Ghosh, R., Santra, S., Ray, S. K. & Guha, P. K. Pt-functionalized reduced graphene oxide for excellent hydrogen sensing at room temperature. *Appl. Phys. Lett.* **107**, 153102 (2015).

9. Imai, Y., Kimura, Y. & Niwano, M. Organic hydrogen gas sensor with palladium-coated beta-phase poly(vinylidene fluoride) thin films. *Appl. Phys. Lett.* **101**, 181907 (2012).
10. Yu, H. M. et al. Capacitive sensor based on GaN honeycomb nanonetwork for ultrafast and low temperature hydrogen gas detection. *Sens. Actuators B* **346**, 130488 (2021).
11. Nugroho, F. A. A. et al. Inverse designed plasmonic metasurface with parts per billion optical hydrogen detection. *Nat. Commun.* **13**, 5737 (2022).
12. Nugroho, F. A. A. et al. Metal-polymer hybrid nanomaterials for plasmonic ultrafast hydrogen detection. *Nat. Mater.* **18**, 489–495 (2019).
13. Kim, S., Singh, G. & Lee, K. K. Development of highly sensitive and stable surface acoustic wave-based hydrogen sensor and its interface electronics. *Adv. Mater. Technol.* **7**, 2200180 (2022).
14. Schefer, T. A. et al. Application of a microfabricated microwave resonator in a Co-Pd-based magnetic hydrogen-gas sensor. *Phys. Rev. Appl.* **18**, 024015 (2022).
15. Kumar, A., Chen, K. W., Thundat, T. & Swihart, M. T. Paper-based hydrogen sensors using ultrathin palladium nanowires. *ACS Appl. Mater. Interfaces* **15**, 5439–5448 (2023).
16. Girma, H. G. et al. Room-temperature hydrogen sensor with high sensitivity and selectivity using chemically immobilized monolayer single-walled carbon nanotubes. *Adv. Funct. Mater.* **33**, 2213381 (2023).
17. Potyrailo, R. A. et al. Extraordinary performance of semiconducting metal oxide gas sensors using dielectric excitation. *Nat. Electron.* **3**, 280–289 (2020).
18. Wang, C. et al. Biomimetic olfactory chips based on large-scale monolithically integrated nanotube sensor arrays. *Nat. Electron.* **7**, 157–167 (2024).
19. Song, Z. L. et al. Wireless self-powered high-performance integrated nanostructured-gas-sensor network for future smart homes. *ACS Nano* **15**, 7659–7667 (2021).
20. Mirzaei, A. et al. An overview on how Pd on resistive-based nanomaterial gas sensors can enhance response toward hydrogen gas. *Int. J. Hydrogen Energy* **44**, 20552–20571 (2019).
21. Favier, F., Walter, E. C., Zach, M. P., Benter, T. & Penner, R. M. Hydrogen sensors and switches from electrodeposited palladium mesowire arrays. *Science* **293**, 2227–2231 (2001).
22. Ranwa, S., Kulriya, P. K., Sahu, V. K., Kukreja, L. M. & Kumar, M. Defect-free ZnO nanorods for low temperature hydrogen sensor applications. *Appl. Phys. Lett.* **105**, 213103 (2014).
23. Yang, S. L. et al. Highly responsive room-temperature hydrogen sensing of alpha-$MoO_3$ nanoribbon membranes. *ACS Appl. Mater. Interfaces* **7**, 9247–9253 (2015).
24. Li, Z., Haidry, A. A., Wang, T. & Yao, Z. J. Low-cost fabrication of highly sensitive room temperature hydrogen sensor based on ordered mesoporous Co-doped $TiO_2$ structure. *Appl. Phys. Lett.* **111**, 032104 (2017).
25. Meng, X. N., Bi, M. S., Xiao, Q. P. & Gao, W. Ultra-fast response and highly selectivity hydrogen gas sensor based on Pd/$SnO_2$ nanoparticles. *Int. J. Hydrogen Energy* **47**, 3157–3169 (2022).
26. Wilken, M. et al. CVD grown tungsten oxide for low temperature hydrogen sensing: tuning surface characteristics via materials processing for sensing applications. *Small* **19**, 2204636 (2022).
27. Cai, Z. & Park, S. Ultrasensitive hydrogen sensor based on porous-structured Pd-decorated $In_2O_3$ nanoparticle-embedded $SnO_2$ nanofibers. *Sens. Actuators B* **367**, 132090 (2022).
28. Naitoh, Y., Sumiya, T., Shima, H. & Akinaga, H. High-speed hydrogen sensor fabricated using a platinum/titanium oxide nanocontact. *Sens. Actuators B* **371**, 132531 (2022).
29. Deshpande, S., Seal, S., Zhang, P., Cho, H. J. & Posey, N. Electrode architecture in tuning room temperature sensing kinetics of nanomicrointegrated hydrogen sensor. *Appl. Phys. Lett.* **90**, 073118 (2007).
30. Liu, B. et al. High-performance room-temperature hydrogen sensors based on combined effects of Pd decoration and Schottky barriers. *Nanoscale* **5**, 2505–2510 (2013).
31. Kong, J., Chapline, M. G. & Dai, H. J. Functionalized carbon nanotubes for molecular hydrogen sensors. *Adv. Mater.* **13**, 1384–1386 (2001).
32. Sun, Y. G. & Wang, H. H. High-performance, flexible hydrogen sensors that use carbon nanotubes decorated with palladium nanoparticles. *Adv. Mater.* **19**, 2818–2823 (2007).
33. Johnson, J. L., Behnam, A., Pearton, S. J. & Ural, A. Hydrogen sensing using Pd-functionalized multi-layer graphene nanoribbon networks. *Adv. Mater.* **22**, 4877–4880 (2010).
34. Al-Mashat, L., Tran, H. D., Wlodarski, W., Kaner, R. B. & Katantar-Zadeh, K. Conductometric hydrogen gas sensor based on polypyrrole nanofibers. *IEEE Sens. J.* **8**, 365–370 (2008).
35. Srivastava, S., Kumar, S., Singh, V. N., Singh, M. & Vijay, Y. K. Synthesis and characterization of $TiO_2$ doped polyaniline composites for hydrogen gas sensing. *Int. J. Hydrogen Energy* **36**, 6343–6355 (2011).
36. Virji, S., Kaner, R. B. & Weiller, B. H. Hydrogen sensors based on conductivity changes in polyaniline nanofibers. *J. Phys. Chem. B* **110**, 22266–22270 (2006).
37. Li, B. C., Lai, P. T. & Tang, W. M. Effects of catalytic-electrode thickness on a hydrogen sensor based on organic thin-film transistor. *Phys. Status Solidi A* **215**, 1700786 (2018).
38. Li, B. C., Lai, P. T. & Tang, W. M. Hydrogen sensors based on TFTs with catalytic source/drain electrodes: IGZO versus pentacene. *IEEE Electron Device Lett.* **39**, 1596–1599 (2018).
39. Abdou, M. S. A., Orfino, F. P., Son, Y. & Holdcroft, S. Interaction of oxygen with conjugated polymers: charge transfer complex formation with poly(3-alkylthiophenes). *J. Am. Chem. Soc.* **119**, 4518–4524 (1997).
40. Lu, C. K. & Meng, H. F. Hole doping by molecular oxygen in organic semiconductors: band-structure calculations. *Phys. Rev. B* **75**, 235206 (2007).
41. Volonakis, G., Tsetseris, L. & Logothetidis, S. Impurity-related effects in poly(3-hexylthiophene) crystals. *Phys. Chem. Chem. Phys.* **16**, 25557–25563 (2014).
42. Grillo, A. & Di Bartolomeo, A. A current–voltage model for double Schottky barrier devices. *Adv. Electron. Mater.* **7**, 2000979 (2021).
43. Buttner, W., Burgess, R., Post, M. & Rivkin, C. *Summary and Findings from the NREL/DOE Hydrogen Sensor Workshop* Report No. NREL/TP-5600-55645 (OSTI, 2012).
44. Li, X. W., Liu, Y., Hemminger, J. C. & Penner, R. M. Catalytically activated palladium@platinum nanowires for accelerated hydrogen gas detection. *ACS Nano* **9**, 3215–3225 (2015).
45. Park, C. H. et al. Hydrogen sensors based on $MoS_2$ hollow architectures assembled by Pickering emulsion. *ACS Nano* **14**, 9652–9661 (2020).
46. Tsetseris, L. & Pantelides, S. T. Intercalation of oxygen and water molecules in pentacene crystals: first-principles calculations. *Phys. Rev. B* **75**, 153202 (2007).
47. Tsetseris, L. & Pantelides, S. T. Oxygen and water-related impurities in $C_{60}$ crystals: a density-functional theory study. *Phys. Rev. B* **82**, 045201 (2010).
48. Van Lent, R. et al. Site-specific reactivity of molecules with surface defects–the case of $H_2$ dissociation on Pt. *Science* **363**, 155–157 (2019).
49. Liao, H. H. et al. Dynamics and reversibility of oxygen doping and de-doping for conjugated polymer. *J. Appl. Phys.* **103**, 104506 (2008).
50. Thomas, K. M. Hydrogen adsorption and storage on porous materials. *Catal. Today* **120**, 389–398 (2007).
51. David, E. & Niculescu, V. C. Volatile organic compounds (VOCs) as environmental pollutants: occurrence and mitigation using nanomaterials. *Int. J. Environ. Res. Public Health* **18**, 13147 (2021).

52. Kresse, G. & Furthmuller, J. Efficient iterative schemes for ab initio total-energy calculations using a plane-wave basis set. *Phys. Rev. B* **54**, 11169–11186 (1996).
53. Blochl, P. E. Projector augmented-wave method. *Phys. Rev. B* **50**, 17953–17979 (1994).
54. Perdew, J. P., Burke, K. & Ernzerhof, M. Generalized gradient approximation made simple. *Phys. Rev. Lett.* **77**, 3865–3868 (1996).
55. Grimme, S., Antony, J., Ehrlich, S. & Krieg, H. A consistent and accurate ab initio parametrization of density functional dispersion correction (DFT-D) for the 94 elements H-Pu. *J. Chem. Phys.* **132**, 154104 (2010).
56. Jepson, O. & Anderson, O. K. The electronic structure of h.c.p. ytterbium. *Solid State Commun.* **9**, 1763–1767 (1971).
57. Momma, K. & Izumi, F. VESTA 3 for three-dimensional visualization of crystal, volumetric and morphology data. *J. Appl. Crystallogr.* **44**, 1272–1276 (2011).
58. Henkelman, G. & Jonsson, H. Improved tangent estimate in the nudged elastic band method for finding minimum energy paths and saddle points. *J. Chem. Phys.* **113**, 9978–9985 (2000).
59. Mandal, S. et al. Protein-based flexible moisture-induced energy-harvesting devices As self-biased electronic sensors. *ACS Appl. Electron. Mater.* **2**, 780–789 (2020).

## Acknowledgements

We thank R. E. Anugrah and G. Pappas for technical support in sensing measurements and S. Shikin for technical help during the atomic force microscopy measurements. This work was supported by baseline funds available to T.D.A. and M.H. and by the Center Partnership Fund of King Abdullah University of Science and Technology. The DFT calculations used the GRNET ARIS HPC resources under project 15002. D.K.G. acknowledges the financial support from the MeitY (5(1)/2017-NANO, 5(1)/2021-NANO) and DST (DST/NM/NNetRA/2018(G)-IIT-KGP).

## Author contributions

S.M. and T.D.A. conceived and designed the experiments. T.D.A. and M.H. guided and supervised the project. S.M. and H.F. set up the gas-sensing platform. S.M. fabricated the organic devices and performed the characterizations (*I*–*V*, *I* versus *t* and atomic force microscopy) and the relevant analyses. S.M. and A.V.M. carried out all the demonstration experiments and collected related data. T.G., S.M. and D.K.G. designed and fabricated the prototype electronics. L.T. performed all the theoretical calculations. S.M., A.V.M. and H.F. outlined and drew the schematics. S.M. wrote the first draft of the paper. All authors discussed the results and commented on the paper.

## Competing interests

A patent related to this work has been filed by inventors S.M., H.F. and T.D.A.

## Additional information

**Extended data** is available for this paper at https://doi.org/10.1038/s41928-025-01352-y.

**Supplementary information** The online version contains supplementary material available at https://doi.org/10.1038/s41928-025-01352-y.

**Correspondence and requests for materials** should be addressed to Suman Mandal or Thomas D. Anthopoulos.

**Peer review information** *Nature Electronics* thanks Zhiyong Fan, Zhilong Song and the other, anonymous, reviewer(s) for their contribution to the peer review of this work.

https://doi.org/10.1038/s41928-025-01352-y

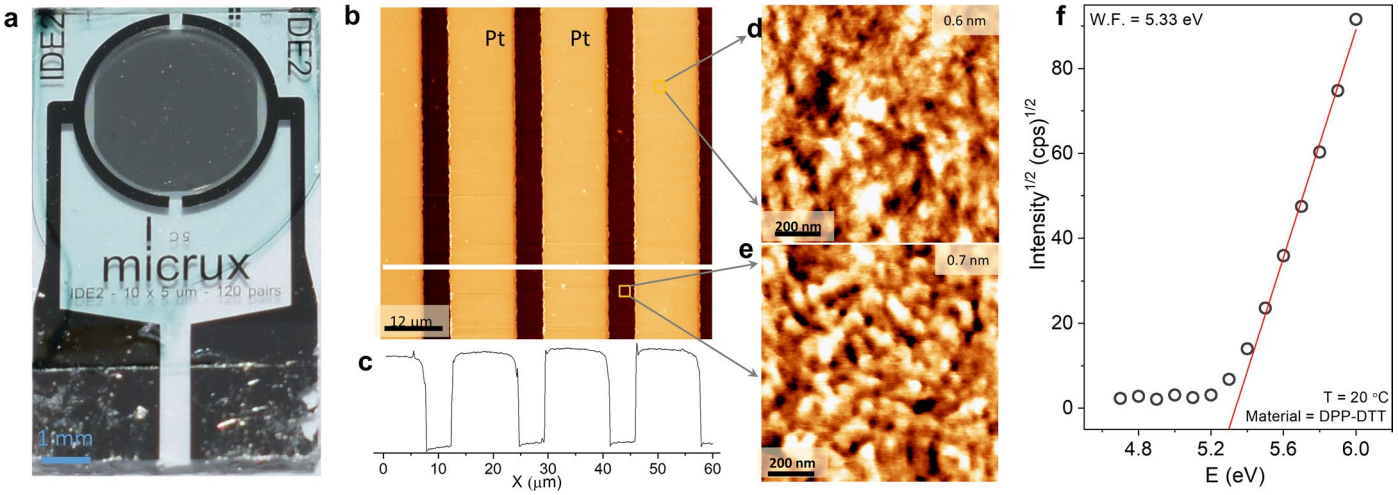


**Extended Data Fig. 1 | Characterisation of organic and platinum thin films.** **a**, Photograph of the organic sensor device with DPP-DTT (light blue) coating the circular interdigitated electrodes region. **b**, AFM-measured surface morphology of the DPP-DTT coated interdigitated platinum electrodes. **c**, Surface profile from the region in (b) marked with a white line. **d**, Surface morphology of DPP-DTT on the Pt electrode. **e**, Surface morphology of DPP-DTT on the glass substrate. **f**, Work function of the Pt electrode measured by PESA.

https://doi.org/10.1038/s41928-025-01352-y

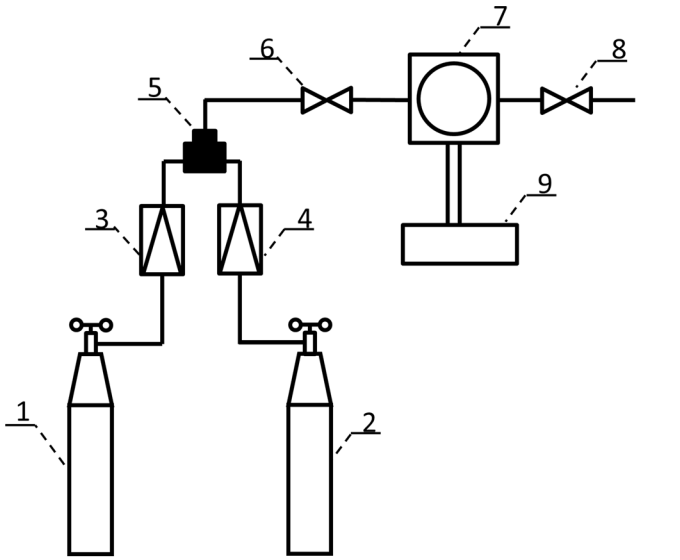


**Extended Data Fig. 2 | Schematic for the gas sensing system used throughout this study.** (1-2) gas cylinders, (3-4) mass flow controllers, (5) gas mixing unit, (6) gas inlet, (7) gas-sensing chamber, (8) gas outlet, and (9) source-measurements unit (SMU).

https://doi.org/10.1038/s41928-025-01352-y

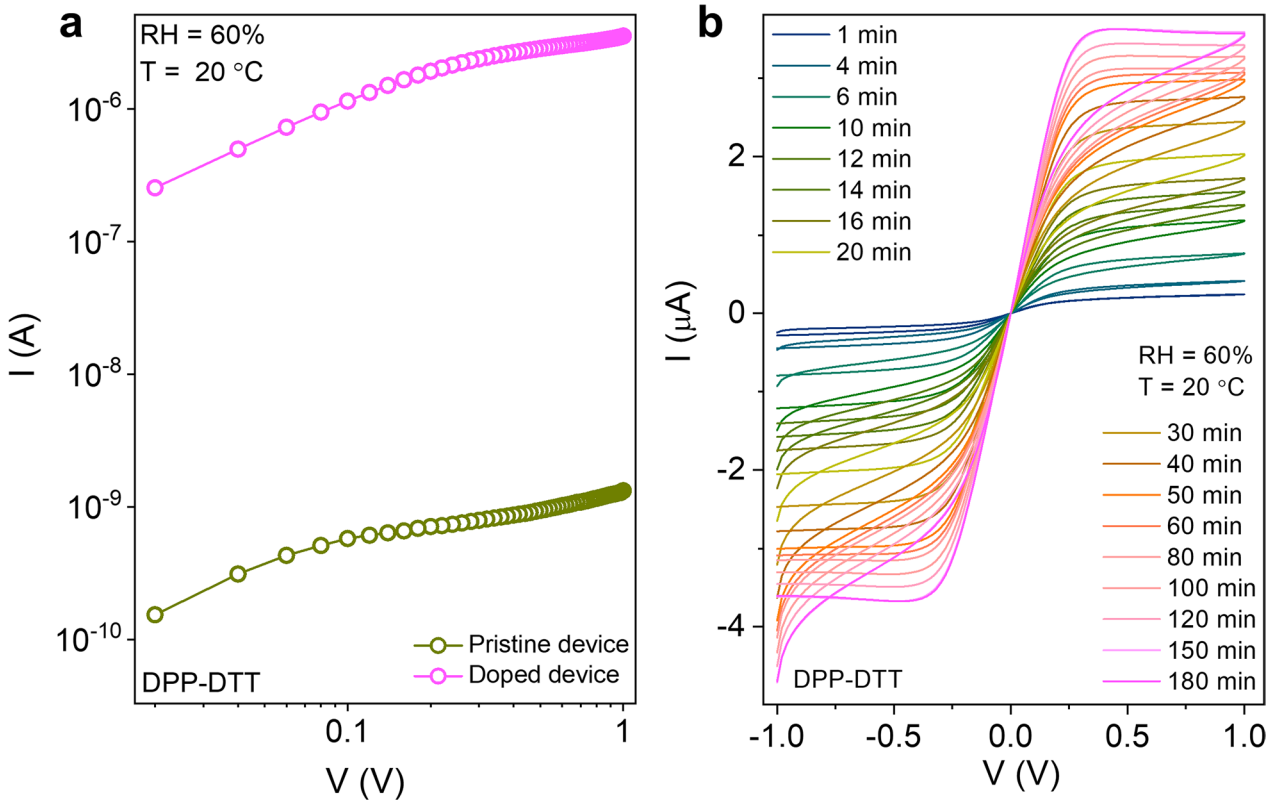


**Extended Data Fig. 3 | Doping effect in the organic semiconductor. a**, I-V curves measured for the DPP-DTT-based device for pristine (before exposure to air) and oxygen-doped devices (after exposure to air). **b**, I-V characteristics taken from the DPP-DTT based device at different time intervals after exposure to air.

https://doi.org/10.1038/s41928-025-01352-y

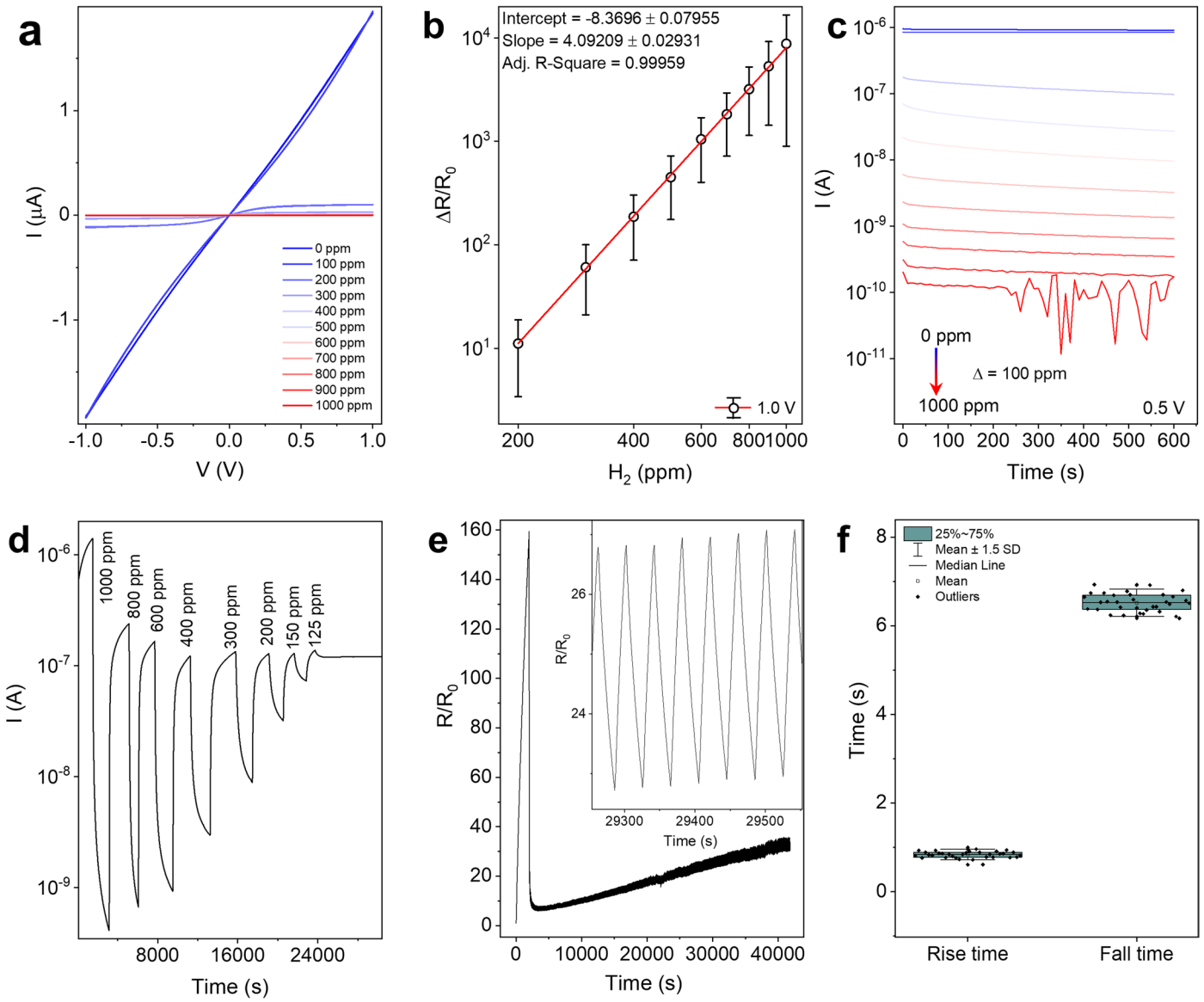


**Extended Data Fig. 4 | Characterisation of the hydrogen sensor.** Hydrogen sensing experiments using interdigitated electrodes coated with DPP-DTT as the sensing material tested at various $H_2$ concentrations from 0 to 1000 ppm. **a**, I-V curves. **b**, $H_2$ concentration-dependent responsivity variation was measured at a constant applied bias of 1.0 V. The error bars indicate uncertainties in the device responsivity mainly stemming from uncertainties in the thickness of the DPP-DTT thin films and represent standard deviation among four individual devices prepared from different batch. **c**, $H_2$ concentration-dependent response variation for a constant applied bias of 0.5 V. The fluctuations after 200 seconds may be due to noise originating from the measurement cables and instruments. **d**, Real-time current evolution upon temporal exposure to $H_2$ at different concentrations measured at a constant bias of 0.5 V. **e**, Device current variation for $H_2$ concentration changes in pulsing conditions from 0 ppm to 1000 ppm at an applied bias of 0.5 V for 1000 cycles. Inset shows a zoomed portion indicating clear hydrogen response. **f**, Rise and fall time calculated from the fast hydrogen response for the 1000 ppm $H_2$ concentration condition. The error bars denote the standard deviation of the mean by averaging over 33 different sensing cycles from a single device.

https://doi.org/10.1038/s41928-025-01352-y

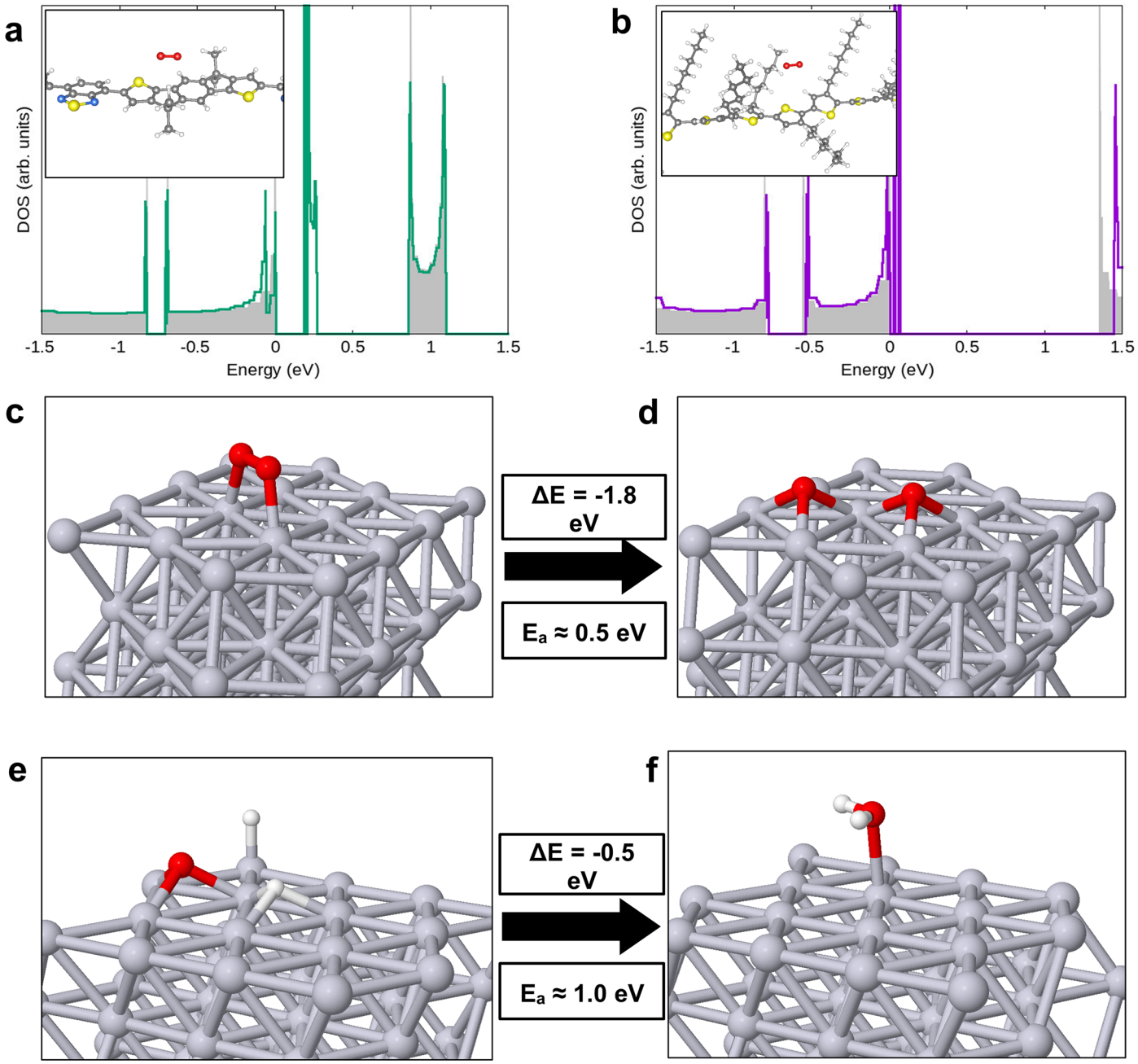


**Extended Data Fig. 5 | Numerical calculation for the interaction of gaseous species (O2 and H2) with organic semiconductors and the surface of the platinum electrode. a**, **b**, Electronic DOS (in arbitrary units) for the pristine $C_{16}$-IDTBT (a), and P3HT (b) polymer chain (grey shaded) and for the $O_2$-physisorbed configuration (green, purple line) shown as an inset (C: grey, H: white, S: sulfur, H: white atoms, N: blue atoms). The energy of the highest occupied state is set equal to zero. The $O_2$-induced peaks above zero (that is, above the valence band maximum) confirm that physisorbed $O_2$ molecules can act as acceptors for the $C_{16}$-IDTBT and P3HT polymer. **c**, **d**, Dissociation of an oxygen molecule on a Pt-(111) surface (c) to a pair of O adatoms on the surface (d) (Pt: grey, O: red atoms). ΔE and $E_a$ are the reaction energy and reaction barriers, respectively. The barrier is small enough to activate the process at RT and produce atomic O species on the surface. **e**, **f**, Reaction between two H adatoms with an O adatom on a Pt-(111) surface (e) and formation of an $H_2O$ molecule (f) (Pt: grey, O: red atoms). ΔE and $E_a$ are the reaction energy and reaction barriers, respectively. The barrier is small enough to activate the process at RT and eliminate O species from the surface.

https://doi.org/10.1038/s41928-025-01352-y

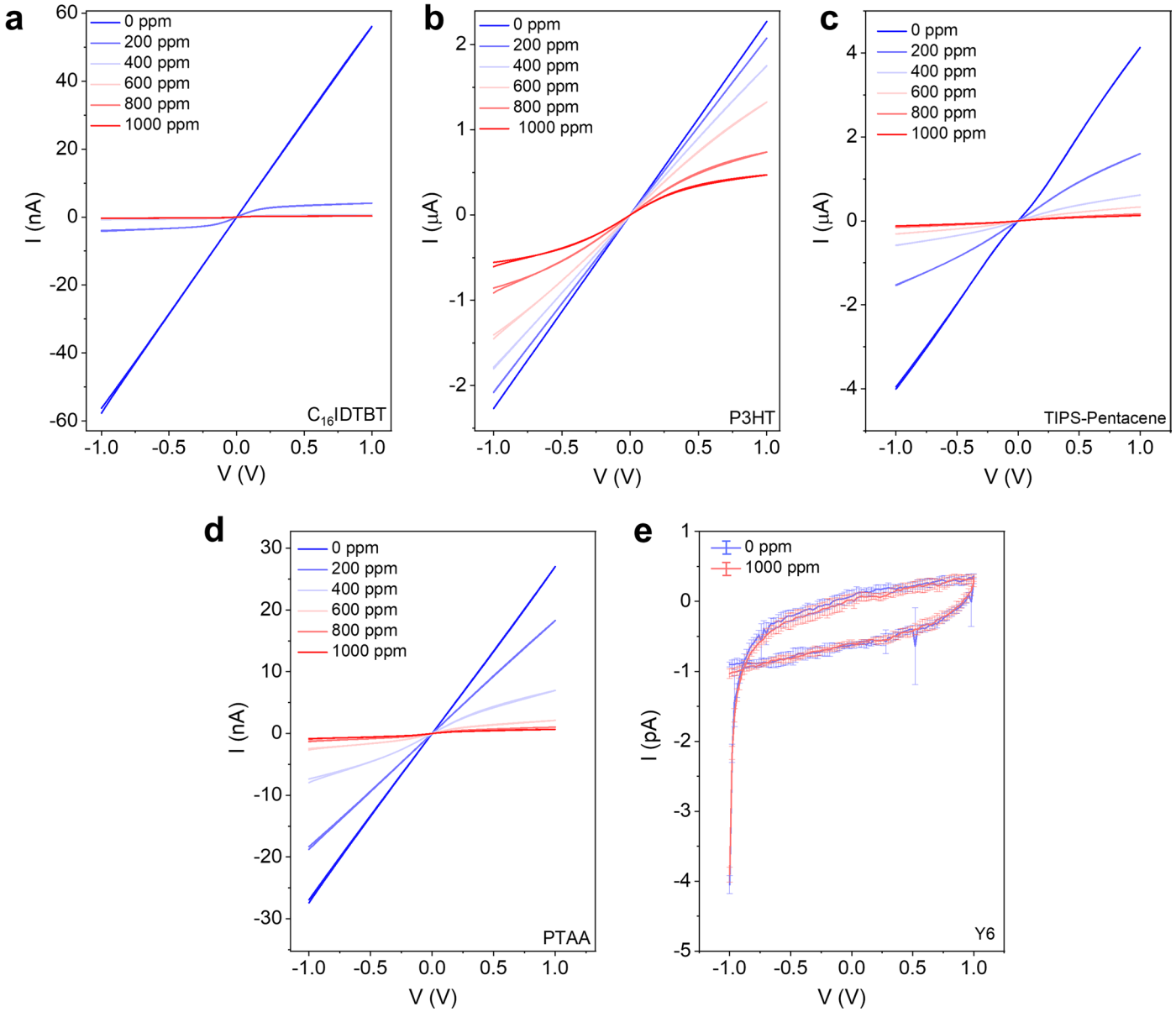


**Extended Data Fig. 6 | Hydrogen response in different organic materials. a-e**, Voltage-dependent current variation in the organic sensor for various $H_2$ concentrations (0-1000 ppm) at 20 °C using DPP-DTT (a), $C_{16}$IDTBT (b), P3HT (c), PTAA (d), and Y6 (e) as sensing materials. The error bars indicate uncertainties in the device current, derived from four sets of measurements on a single device.

https://doi.org/10.1038/s41928-025-01352-y

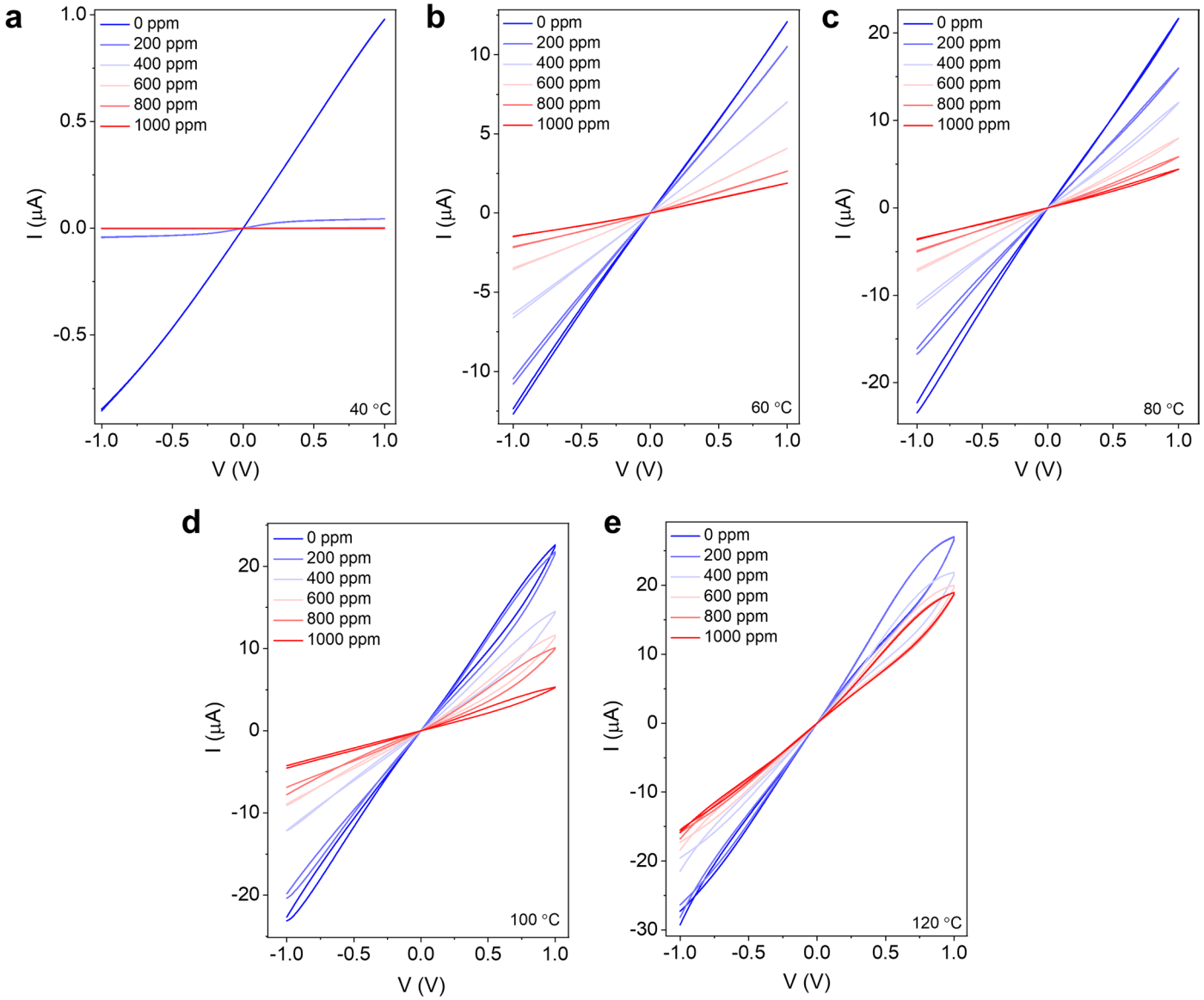


**Extended Data Fig. 7 | Temperature-dependent hydrogen response. a-e**, Voltage-dependent current variation using DPP-DTT based sensor for various $H_2$ concentrations (0-1000 ppm) at 40 °C (a), 60 °C (b), 80 °C (c), 100 °C (d), and 120 °C (e).

https://doi.org/10.1038/s41928-025-01352-y

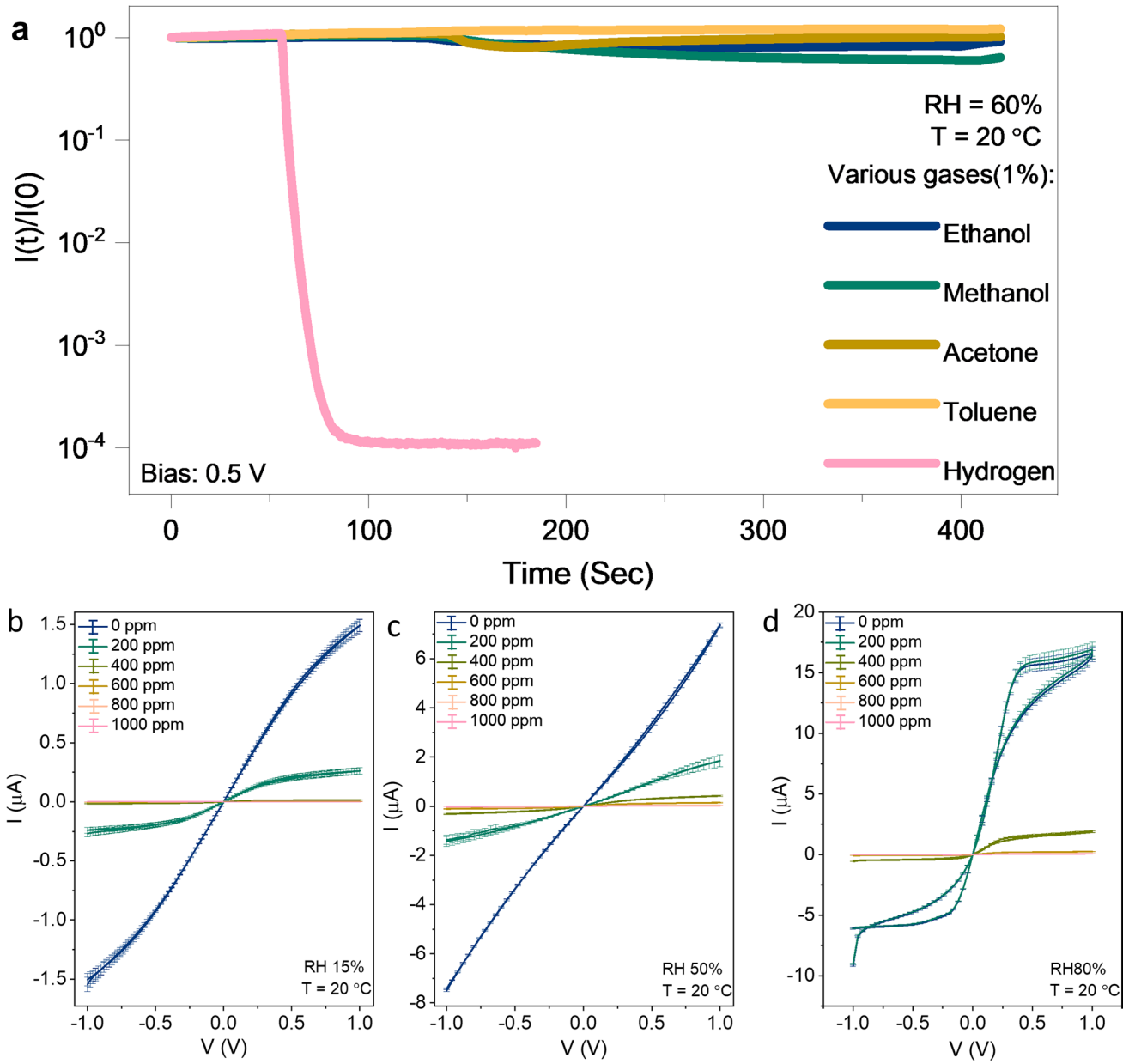


**Extended Data Fig. 8 | Hydrogen sensing characteristics measured from an interdigitated DPP-DTT sensor under various volatile gases and RH conditions at 20 °C. a**, Normalised current response for various volatile gases at a concentration of 1% measured at 0.5 V from interdigitated electrodes using DPP-DTT as the sensing material at 20 °C. **b-d**, Current-voltage characteristics for various $H_2$ concentrations ranging from 0 to 1000 ppm in increments of 200 ppm measured at various RH conditions 15%, 50% and 80% RH, respectively. Error bars denote the standard deviation for the I-V characteristics obtained from four measurements from the same device.

https://doi.org/10.1038/s41928-025-01352-y

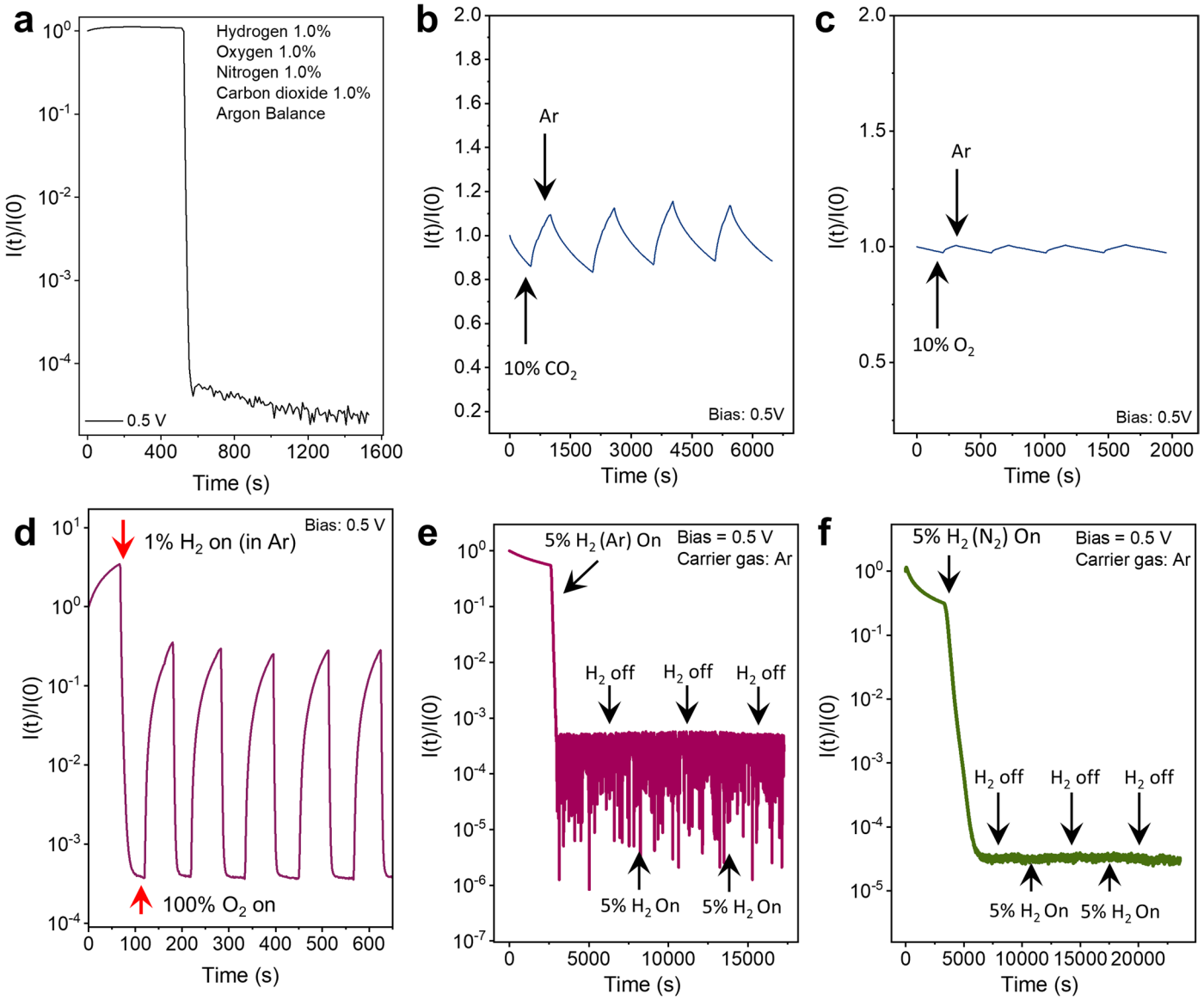


**Extended Data Fig. 9 | Various gas responses using the organic sensor measured at room temperature. a**, Demonstration of selective hydrogen sensing from a gas mixture that contained 1.0% $H_2$, 1.0% $O_2$, 1.0% $N_2$, and 1.0% $CO_2$ with balance Ar. **b**, **c**, Time-dependent current evolution of the organic sensor in the presence of 10% carbon dioxide ($CO_2$) (b), oxygen ($O_2$) (c) gas where Ar was used as carrier gas at 20 °C measured at 0.5 V. **d**, Real-time current response in the presence of $H_2$ (~1%) and $O_2$ (100%). Real-time response of a DPP-DTT sensor to $H_2$ using Ar or $N_2$ as the carrier gases measured at 20 °C. **e**, **f**, Device current response when 5% $H_2$ (Ar) (e) and 5% $H_2$ ($N_2$) (f) were used as sensing gases. The carrier gases in (e) and (f) were Ar and $N_2$, respectively.

https://doi.org/10.1038/s41928-025-01352-y

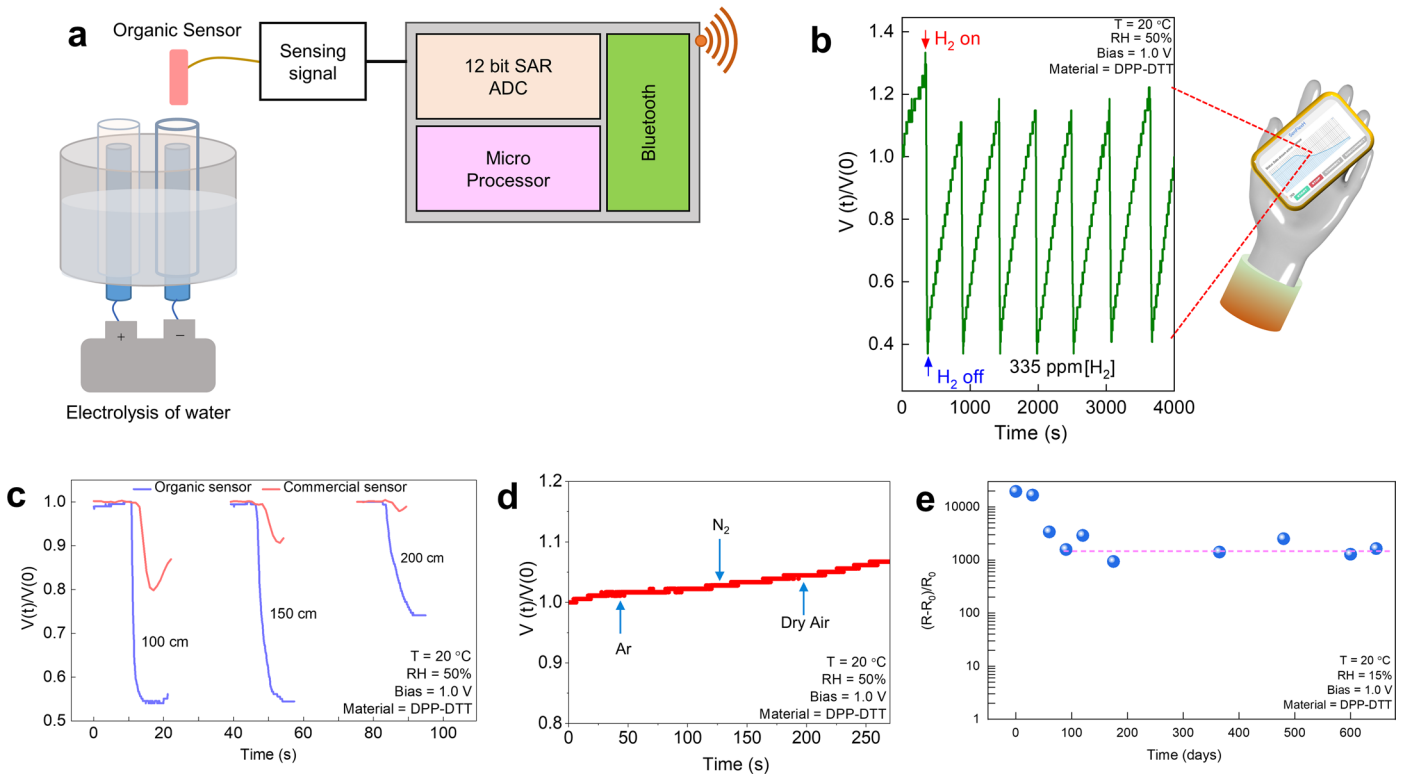


**Extended Data Fig. 10 | Practical demonstrations of hydrogen sensing and long-term stability of the organic sensor. a**, Schematic of the water electrolysis setup with prototype electronics and the organic hydrogen sensor. The data was collected wirelessly on an Android mobile using a dedicated application software. **b**, Time-dependent normalised voltage response from the generated hydrogen recorded remotely by a smartphone via Bluetooth. **c**, Comparisons of the hydrogen sensing response between the organic and a commercial sensor during the balloon burst experiments. Before popping with a needle, the sensors were placed at different distances (100, 150, and 200 cm) from the 100% hydrogen-filled balloon. The normalised voltage response with time from the sensors reflects a better performance in our DPP-DTT-based sensor than the commercial sensor. **d**, Demonstration of the response in output voltage measured with time in ambient from the organic sensor using prototype electronics in a balloon bursting experiment using balloons filled with Ar, $N_2$, and dry air placed 100 cm from the organic sensor. **e**, Responsivity of a DPP-DTT sensor recorded at 1 V bias during intermittent brief exposures (1-5 min) to 1000 ppm hydrogen over 646 days. These measurements were performed while the organic sensor was kept at 20 °C with 15% RH. Between measurements, the sensor was stored inside a drawer in the dark at ambient conditions (50-60% RH at 20-24 °C).